

EXPERIMENTAL CHARACTERISTICS OF WIND TURBINE BLADING OVER FULL 0 TO 360 DEGREE ANGLE OF ATTACK

April 2014

Project Number : RD-RD-400-11



Dr. A.P. Haran
Prof. Soundranayagam
Prof.J.J. Isaac

Professor, H.O.D
Professor
Professor

Department of Aeronautical Engineering
Park College of Engineering and Technology
Anna University
Kaniyur, Coimbatore -641659

NOTICE

This report was prepared as an account of the work sponsored by Centre for Wind Energy Technology (C-WET). Neither C-WET nor any of their employees, makes any warranty, express or implied, or assumes any legal liability or responsibility for the accuracy, completeness, or usefulness of any information, apparatus, product, or process disclosed, or represent that its use would not infringe privately owned rights. Reference herein to any specific commercial product, process, or service by trade name, trademark, manufacturer, or otherwise does not necessarily constitute or imply its endorsement, recommendation, or favoring by C-WET. The views and opinions of authors expressed herein do not necessarily state or reflect those of C-WET.

No part of this report shall be either reproduced or otherwise be used in any form without the written permission of the C-WET and the proponent.

Available electronically at <http://www.cwet.res.in>

EXPERIMENTAL CHARACTERISTICS OF WIND TURBINE BLADING OVER FULL 0 TO 360 DEGREE ANGLE OF ATTACK

April 2014

Project Number : RD-RD-400-11



Dr. A.P. Haran
Prof. Soundranayagam
Prof.J.J. Isaac

Professor, H.O.D
Professor
Professor

Department of Aeronautical Engineering
Park College of Engineering and Technology
Anna University
Kaniyur, Coimbatore -641659

ACKNOWLEDGEMENTS

The Centre for Wind Energy Technology (C-WET) would like to acknowledge the experts from Park College of Engineering and Technology, Anna University, Kaniyur, Coimbatore – 641 659, who have authored this report. C-WET also thanks the Ministry of New and Renewable Energy (MNRE) for their financial and technical support for the research and production of this report.

Major contributors in alphabetical order include :

Dr. A.P. Haran	Professor, H.O.D
Prof. Soundranayagam	Professor
Prof.J.J. Isaac	Professor

CHAPTER NO.	TITLE	PAGE NO.
1.	INTRODUCTION	1
2.	EXPERIMENTAL SETUP AND CALIBRATION	1
3.	EXPERIMENTAL VALIDATION	3
4.	AEROFOILS PERFORMANCE CHARACTERISTICS	5
4.1	BLADE LOCATION IN THE TEST SECTION	5
4.2	CONFINED FLOW ANALYSES	
	[CLOSED TEST SECTION]	5
4.3	ANALYSIS WITHOUT CONFINEMENT:	
	[HALF OPEN TEST SECTION]	7
	4.3.1 NWT 1001	7
4.4	NWT 2004	9
4.5	NWT 2005	11
5.1	LIFT AND DRAG AT DEEP-STALL ANGLES	12
6.1	CONCLUSION	13
7.1	REFERENCES	15

APPENDIX -I

1	C_p PLOT FOR VARIABLE ANGLES ATTACK WITHOUT CONFINED FLOW NWT 1001	16
2	C_p PLOT FOR VARIABLE ANGLES OF ATTACK [NWT 2004]	30
3	C_p PLOT FOR VARIABLE ANGLES OF ATTACK [NWT 2005]	40

NOMENCALURE

p	Static pressure on the aerofoil surface
p_{∞}	Reference pressure
ρ	Density of air
V_{∞}	Free stream velocity
α	Angle of attack
R	Resaultent force
L	Lift
D	Drag
N	Normal force
A	Chord wise force
C_p	Local pressure co efficient
C_l	Co efficient of lift
C_d	Co efficient of drag
C_n	Co efficient of normal force
C_a	Co efficient of chord wise force
Re	Reynolds number

1. Introduction

Most of the wind turbines in our country are based on imported technology and design. It is often felt that their performance characteristics are not well suited to the Indian wind regime. Since India is one amongst the world leaders in harvesting wind power, it is important that the wind turbine used in India should be suitable to the Indian wind condition and be based on indigenous technology. Hence, the information would be of special importance in the design of stall regulated wind machines. Special attention should be paid to the flow regime immediately around the stall point and at high angles of attack. This knowledge is essential for the understanding of its starting capability and low speed performance. But in India the resources about the high angle of aerodynamics is limited, hence this experimental study would be of great importance to wind turbine designers.

Blade profiles designed for a particular capacity of wind turbine by National Aerospace Laboratories viz, as NWT1001, NWT2004, NWT2005 Tip section, mid span and Root section of the blade respectively were obtained and used for the experiment and CFD simulation. the blade profiles are showing in figure 1(a). The above blading belonged to the stall regulated class of wind turbine. An indigenous wind turbine blading has been evaluated for angles of attack ranging from 0° to 360° using low speed wind tunnel. The wind turbine performance can normally be predicted through the use of the blade element momentum theory together with two dimensional aerodynamic data. This method has been used to obtain lift and drag characteristics of the blade from the data obtained from the wind tunnel testing. The wind turbine blades are tested at give a Reynolds number around 200,000 which is far above the critical Reynolds number of similar airfoils for angles of attack varying from 0° to 360° .

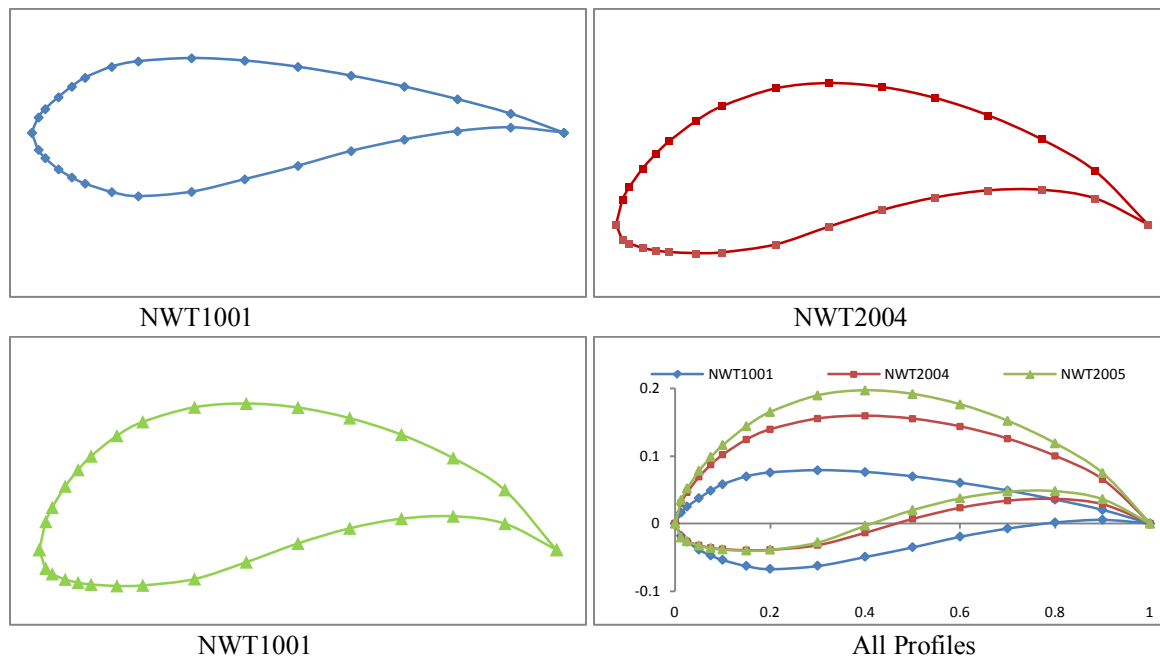


Figure 1(a): Wind turbine profiles

2. Experimental set up and calibration

The experiments were performed in a blower type low speed wind tunnel. The centre line height is 48 inches (1200 mm) which is very convenient for most experimental purposes. A centrifugal blower draws air from the room and delivers it horizontally into a long straight diffuser. A vertical central splitter approximately one of the diffuser lengths is installed at diffuser inlet. The flow from the diffuser enters a 6feet x 6feet (1830mm x 1830mm) plenum chamber where it passes through a honeycomb and a set of wire screens before entering the test section to provide uniform flow with low turbulent intensity. The general purpose test section has Perspex side walls and plywood roof and floor. The flow leaving the test section is left free to the outside atmosphere. A large filter box lined with fine muslin, about 2000 mm cube can be fitted to enclose the blower inlet to minimize dust interference with hot wire probes. The general purpose test section is 24inches (610 mm) square and 5feet (1525 mm) long.

The tunnel calibration was done to capture the wall boundary layer thickness which was found to be 15 mm from each wall of the tunnel. The turbulence intensity in the test section was measured using Hot Wire Anemometer and found to be 0.7% at maximum velocity of wind tunnel.

The pressure distribution over the blade was measured using 32-channel SCANIVALVE pressure sensors. The model is placed along the centreline of the test section with the help of the mounting arrangement. An indexing disc which permits rotation of the blade through 360° in one degree step, is placed and tightened on top of the model over the test section of the tunnel. The photo of the indexing mechanism is shown in figure 1(b).



Figure 1(b): Indexing arrangement.

3. Experimental validation

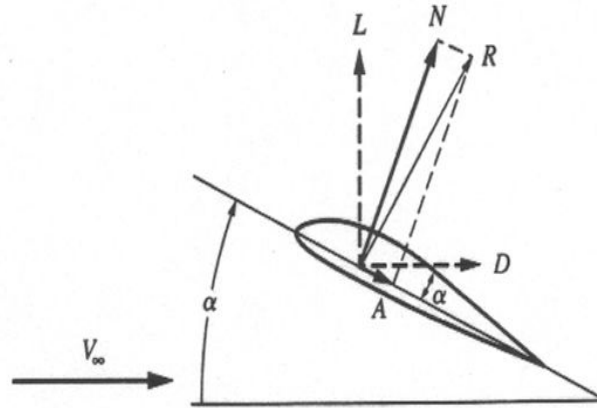


Figure 2. Forces acting on the aerofoil

Figure 2. shows forces acting over an aerofoil. Based on the pressure measurements on the suction side and pressure side, pressure coefficient is calculated using the formula given below and plotted against x/c i.e. along the chord for different angles of attack. The c_p distributions obtained for various angles of attack are shown in figure 3(a). The airfoil characteristics obtained from the experiments for angles of attack up to 16 degree are compared with CFD results. As the results are comparable, experiments were conducted for the rest of the angle of attack up to 360 degree.

$$C_p = \frac{2(p - p_\infty)}{\rho V_\infty^2}$$

Figure 3(b) shows the plot of pressure co efficient against chord wise direction for the angle of attack of 8° . There is a good match between the experiment and the CFD results. The flow separation noticed at 18 % of the chord in the suction surface of the blade has been predicted by CFD and is shown in Figure 3(c).

Lift and drag co efficient were estimated using the following formulae. C_n and C_a are calculated by integrating the pressure coefficient along the chord and the normal to the chord respectively.

$$C_l = C_n \cos \alpha - C_a \sin \alpha$$

$$C_d = C_n \sin \alpha + C_a \cos \alpha$$

Figures 4 and 5 show the variation of lift and drag co efficient with α . Estimated values of lift and drag co efficient obtained from the experiments for angles of attack up to 12 degree, the angle of attack prior to stalling, agree well with the CFD predictions. Beyond stall lift and drag do not match with CFD results because the flow becomes largely separated. The turbulence is modelled and validated using the results obtained from the attached flow and mildly separated flow experiments. Hence these models are very poor in predicting highly separated flows for angles of attack beyond stall.

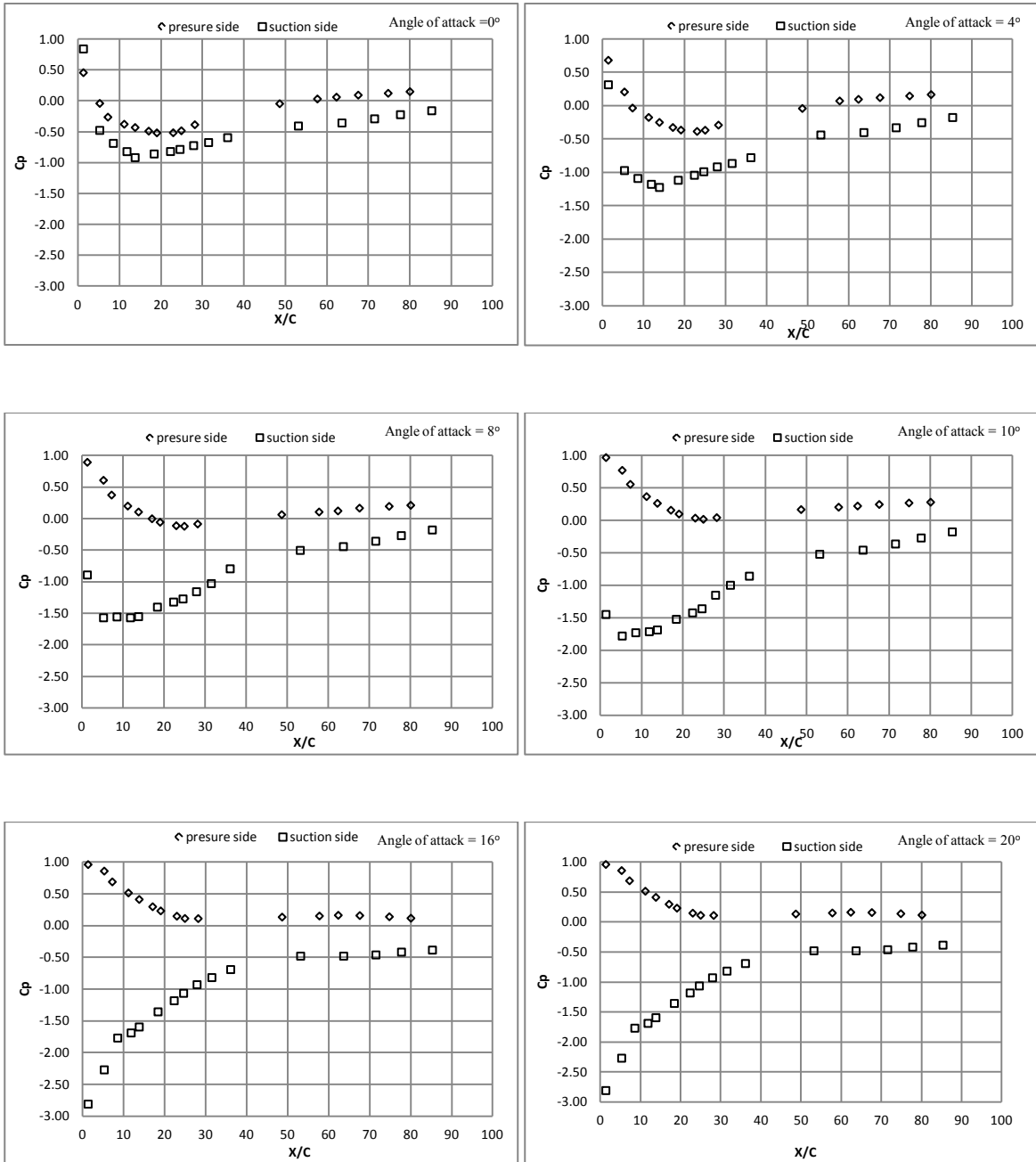


Figure 3(a): Pressure Distribution over the aerofoil for angles of attack from 0 to 20 degree

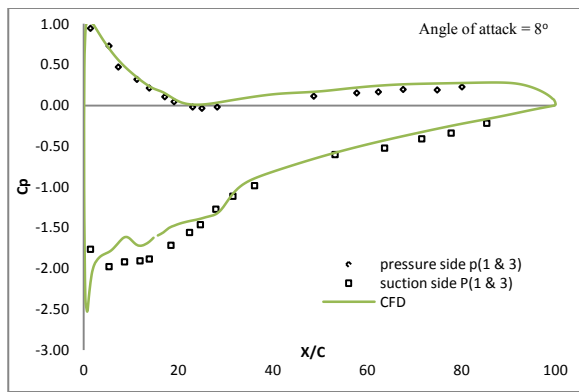


Figure 3(b): Pressure distribution over the airfoil

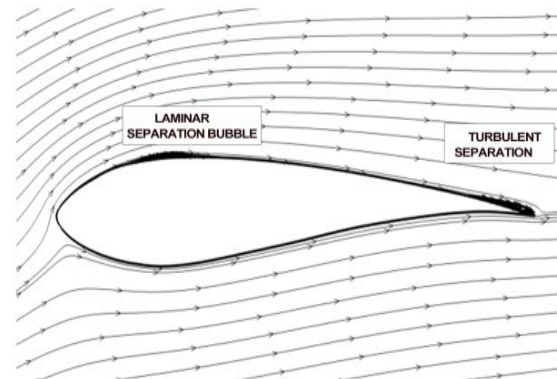


Figure 3(c): Computed streamlines on NWT 1001

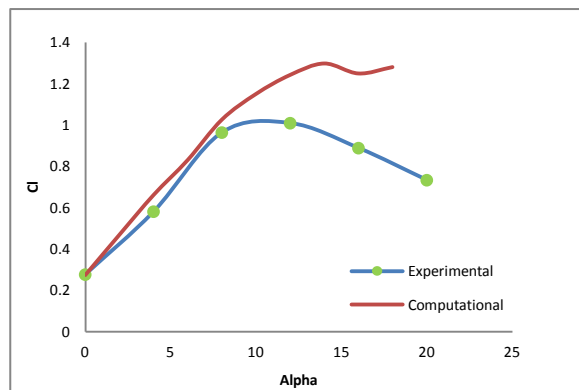


Figure 4: Co efficient of lift vs. Alpha

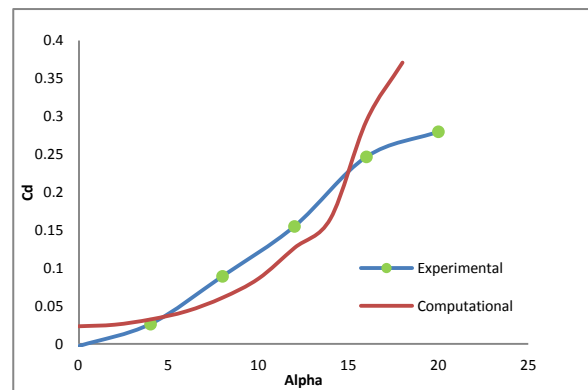


Figure 5: Co efficient of drag vs. Alpha

4. Aerofoils Performance Characteristics:

4.1. Blade Location in the Test Section:

The detailed experimentation was done for all the blades in the open i.e. the blades were kept two chord downstream of the exit of the test section. In this position, the flow field will face minimum confinement and hence mimics the actual flow condition.

To differentiate between the performance of the blade in the free flow field and confined flow field, NWT1001 blade was tested by mounting the blade inside the test section, wherein the walls of the test section confine the flow around the blade. Under confined conditions, the blockage to the flow increases with increasing angles of attack, reaching a maximum of 25 percentage at 90 degree and as per Rainbird^[2] observations in the wind tunnel, measured $C_{L\ max}$ and $C_{D\ max}$ are higher by 20%

4.2. Confined Flow Analysis [Closed test section]:

Performance of the blade (NWT 1001) in term of Cl and Cd is evaluated by measuring the blade pressure distribution for different angles of attack. The cp distributions are shown in appendix - I. The blade pressure distribution is obtained by chord wise distributed pressure taps

of 0.8 mm diameter over the suction and pressure faces. Lift and drag co-efficients NWT1001 were estimated for angles of attack varying from 0° to 360° presented in figure 6, at Reynolds number 200 000. As expected, it can be seen that the lift curve linearly increases and the maximum co efficient occurs at 12° angle of attack. There-after it falls and then rises up to 44° . The cause of decrease in lift coefficient is due to unsteadiness over the aerofoil due to separation at the trailing edge of the section side. Due to the constrained flow field, the airflow on the suction side reattaches causing an increase in the lift coefficient up to 44° angle of attack. With the increase in incidence beyond 44° , the flow is fully separated over the entire aerofoil suction surface causing the lift co-efficient to fall rapidly to a negative value of 0.9 at an alpha of 140 degree from zero at 92 degree angle of attack. This position corresponds to a flat plate facing the flow at right angles to the surface. With incidence further increasing lift co efficient rises steadily from -0.9 to zero at an angle of attack of 180° .

Now, the trailing edge of the blade is facing upstream flow and it is creating the pressure difference over an aerofoil which causes the lift co efficient rise to a value of 0.55 at an angle of attack of 188° . Any further increase in the angle of attack causes a reproduction of the C_L curve but the maximum value of lift co efficient in this segment reaching 0.8 as against to 1.3 where leading edge is facing the flow.

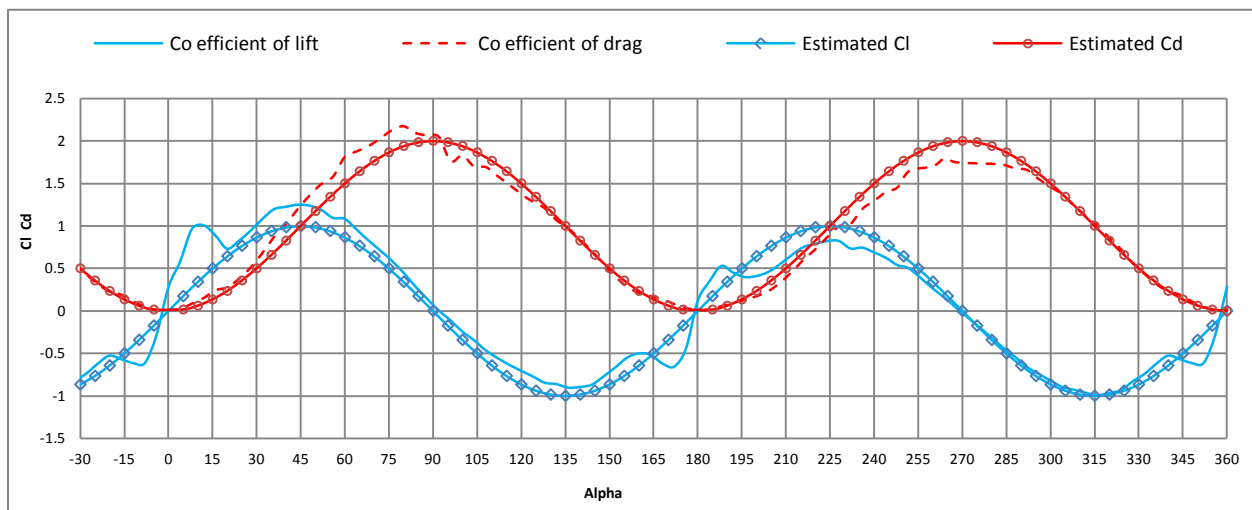


Figure 6: Closed test section Cl and Cd(NWT 1001) blade.

The drag co efficient plot with alpha is close to a sinusoidal curve, the lower value at the trough occurring at zero degree angle of attack ($C_d = 0.02$), 180° and 360° angle of attack and the peak values occurring at 82° ($C_d = 2.08$) and at 272° angle of attack. At these angles of attack the aerofoil acts like a bluff body (flat plate) causing complete breakdown of the flow and creates a large re-circulating zones behind the airfoil.

The Lift and Drag co efficient curves plotted from the experimentally derived values and estimated from the following formulae match very well indicating the accuracy of the

experimental results. The estimated values are derived from the flat plate theory. The results are matching only at high angles of attack because at lower angles of attack the blade is behaving like aerofoils but at high angles of attack this profile is behaving like a flat plate.

$$C_l = \sin 2\alpha$$

$$C_d = 2 \sin^2 \alpha$$

The important observation in the lift curve is that the post stall C_L value ($C_L=1.25$) is greater than the first-stall peak value of 1.0. This kind of phenomena never occurs in the real flow field over an aerofoil. And hence, it is attributed to the effect of confined flow over the blade.

4.3 Analysis without Confinement: [Half open test section]

4.3.1 NWT 1001

As per the recommendations of Rainbird^[3] to avoid wall effects at high incidences the blade was kept outside of the wind tunnel, one and half feet away from wind tunnel test section, that is to say half open test section was used. Figure 7 shows the variation of estimated lift and drag co-efficient with angles of attack. This continuous increase of lift coefficient with angle of attack matches very well with the variation of lift coefficient in the confined flow up to pre-stall (first peak). In the post stall regime, the lift coefficient slightly differs from the closed wall analysis with the second peak reaching 0.97 as against 1.22 in the closed flow tunnel. There-after there is no significant difference in the free flow analysis. Eventually with higher angles of attack, the fully separated flow over suction surface of the aerofoil leading to a decrease in lift coefficient followed by a sudden drop occurring at 68° through 72°, i.e. C_L value dropping to 0.31 from 0.59. This is an indication of the starting point of the separation bubble suddenly moving towards the leading edge causing total flow separation on the suction surface. There-after the drop in lift coefficient is gradual up to 112°. At 112° the drop is sudden once again. The C_L value drops from -0.15 to -0.42.

As expected, in the post-stall regime, the flow is completely separated on the suction surface of the aerofoil. It can be seen in figure 8. Almost the pressure coefficient is constant on the suction side but the values differ with increasing angles of attack. There is a sudden variation in the suction side pressure coefficient, with increasing angles of attack, which in turn leads to changes in lift and drag coefficients. At 68° angle of attack, the flow on the suction side turns over the leading edge before the onset of separation. At 72° angle of attack, the flow deviates away from the suction surface creating a larger wake region. The drag coefficient curve, as expected, starts off as a sine curve from 0° angle of attack but deviates from the curve with a sudden drop at 68° through 72°. Again it follows the sine curve till 112° where it shoots up through 116° and then follows the sine curve. This phenomenon is well known and is called the drag bucket.

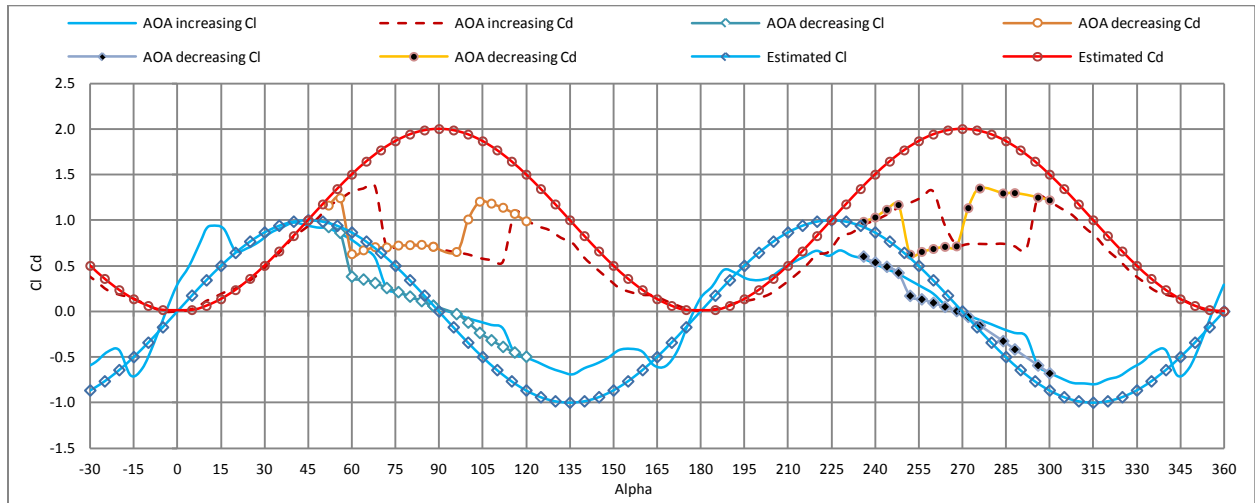


Figure 7: Open test section C_l and C_d Aerodynamics data (NWT 1001)

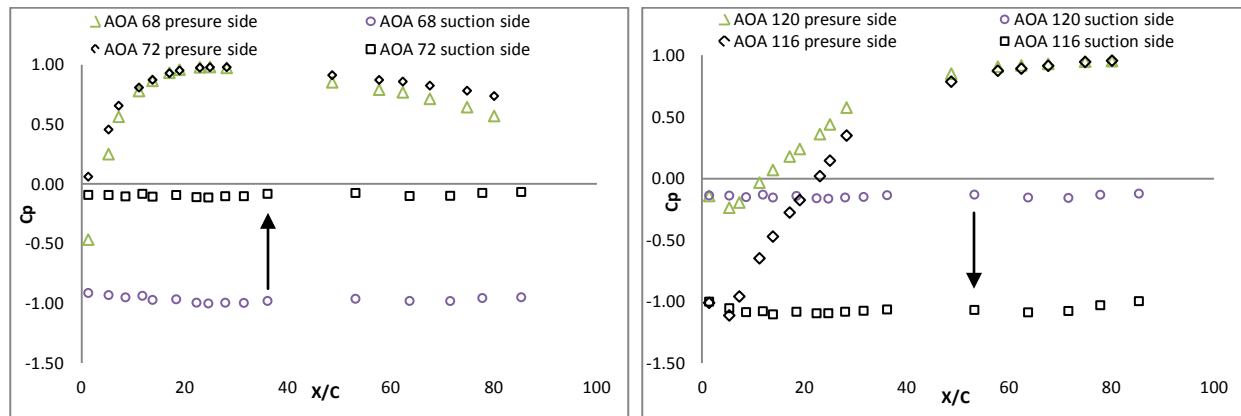


Figure 8: Pressure distribution over the aerofoil NWT 1001 for open section.

The sudden changes in lift and drag coefficient can be explained with the help of pressure distribution and hence C_p over the chord length. The change in the pressure distribution over the pressure surface is marginal, whereas it is flat and marked over the suction surface. The change in area of the curve over the angle of attack is large enough to give a large change in lift and drag coefficient. Similar trend follows for all angles of attack above 180° .

Another important feature to observe is the hysteresis loop in the C_L and C_D characteristics. While repeating the test by lowering the angle of attack from 180° to 0° , C_D rose up to 112° followed by a sudden drop at 112° through 102° . Thereafter the trend continues up to 60° at which it rises suddenly from 56° through 52° before following the sine curve. Similar trend is captured in the C_L curve.

Surprisingly the hysteresis loop occurs in the deep stall region instead of in the stall region, as reported in the literature^[4]. Due to the existence of multiple values of C_L and C_D for a given angle of attack in the hysteresis loop, the airflow over the blade will be unsteady causing

violent oscillations and hence fatigue. These regions should be taken care during the design and if not possible to avoid during the design, the operation in this region is to be avoided totally. If these blades are meant for vertical axis machines, the blades will be exposed to the hysteresis loop during every rotation and hence such a design is not recommended for vertical axis machines.

4.4. NWT 2004

The NWT 2004 aerofoil exhibits, as shown in figure 9(a), both a higher lift peak and slightly more progressive and delayed stall compared with NWT 1001. In this case, stall occurs at 20° angle of attack with a C_L value of 1.58. Beyond stall C_L drops up to 28° angle of attack and then rises to reach a peak value of 1.27 at 32°. Thereafter it follows a similar trend and it closely resembles the C_L curve of NWT 1001.

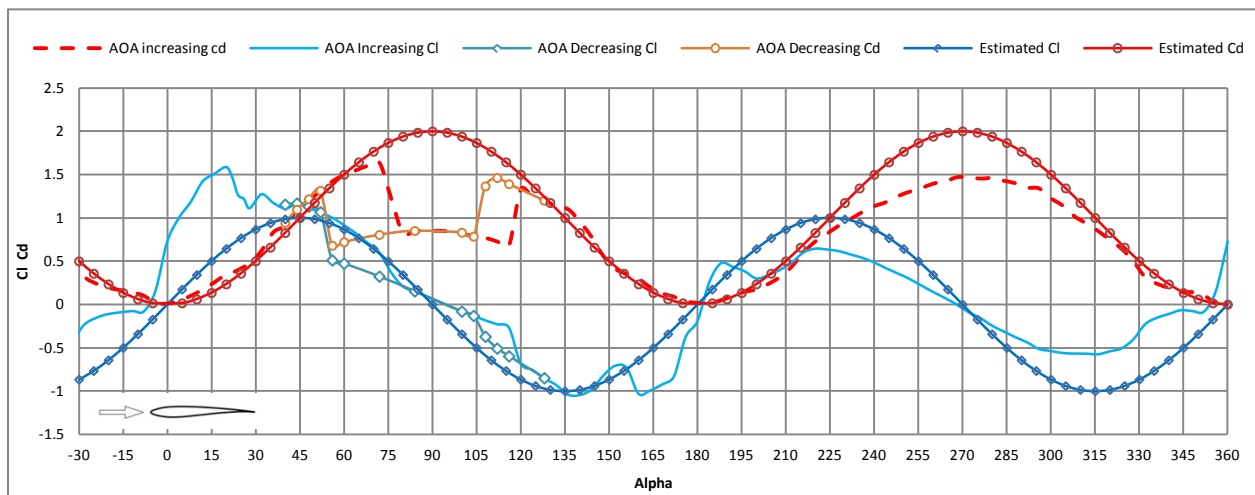


Figure 9(a): Open test section C_L and C_D Aerodynamics data (NWT 2004).

At 52° incidence, the separation bubble bursts causing separated flow occupying the complete suction surface. Similar drop occurs at an angle of 104° incidence. This flow behaviour is analogous to NWT 1001. While conducting the tests with decreasing incidence the hysteresis loop appears in both the C_L and C_D curves. The third and fourth loops observed in the NWT 1001 beyond 180° are not seen in this aerofoil (NWT2004).

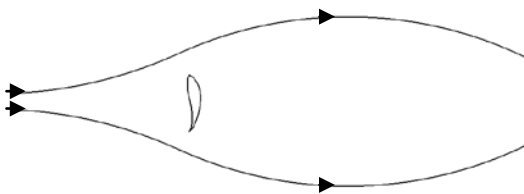


Figure 9(b): Flow over an aerofoil NWT2004 at 90°

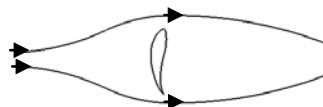


Figure 9(c): Flow over an aerofoil NWT2004 at 270°

The above phenomena can be explained using Figure 9 (a) and (b). The pressure /flat is facing the flow when the angle of attack is around 90° . As a result the flow around the aerofoil is similar to a wake behind a flat plate, whereas at around 270° the suction/curved surface of the aerofoil meets the flow, thereby giving time for the flow to negotiate over the curved surface. This creates a comparatively small wake region with less curvature due to this reason; the flow is not separated completely and rather closer to the surface in the downstream of the aerofoil.

Figure 10 shows the pressure distributions over the aerofoil at various angles of attack. At 0° the separation bubble is found on both the sides of the aerofoil. The location of the separation bubble on the pressure side is from x/c 0.15 to 0.43 and from x/c 0.67 to 0.82 on the suction side. The separation bubble on suction side is not seen at 4° angle of attack. Even though the bubble is present on pressure side, the separation point is moved towards the trailing edge of the aerofoil. The size of separation bubble is shrunk and lies between x/c 0.45 to 0.54. For further increase in angle of attack the bubble gets smaller and completely suppressed at 12° angle of attack.

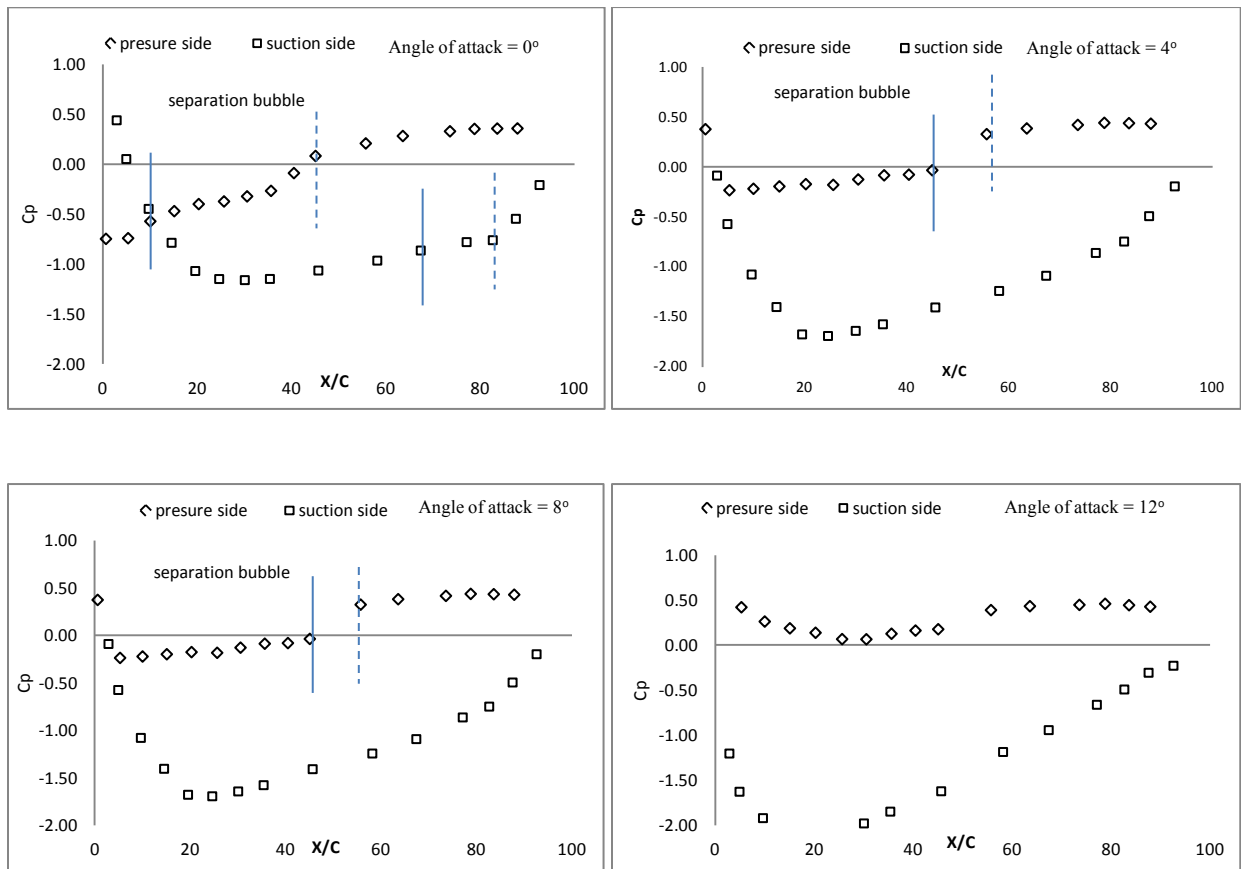


Figure 10: Pressure distribution over the Aerofoil for NWT 2004.

4.5. NWT 2005

The lift and drag characteristics of the NWT2005 aerofoil are shown in figure 11 and it can be seen that, it closely resembles that of NWT2004 lift and drag curves. With increasing angles of attack lift coefficient increases linearly reaching a peak value of 2.05 after which it drops. The stall is delayed as compared to the other two aerofoils. NWT2005 aerofoil is highly cambered as compared to other two profiles. Hence, the profile is able to turn the flow even at higher angles of attack.

Beyond stall, the flow is separated on both the suction and pressure surface as can be seen in the pressure distribution in figure 12. The pressure distribution shown in fig 12 indicates separation bubbles near the trailing edge on the pressure surface and at 20% of the chord on the suction surface at 0° angle of attack. At 8° incidence the separation is seen in the leading edge on the pressure surface. At 28° the separation bubble is seen on the trailing edge of the suction surface and most part of the pressure surface. At 32° the flow remains attached up to 40% of the chord on the suction surface and 20% of the chord on the pressure surface. With increase in angle of attack from 0° to 28° the area within the pressure distribution keeps increasing with a corresponding increase in C_L .

Although, at some high angles of attack there are discontinuities in lift and drag coefficients, and this kind of phenomena has already been discussed with reference NWT2004. In this case, this discontinuity lies between 72° to 120° angles of attack. The C_l and C_d curves obtained while decreasing the angle of attack join the parent C_l and C_d curves over a large range angle of attack as compared to NWT2004 where the C_l and C_d curves join parent curves sharply

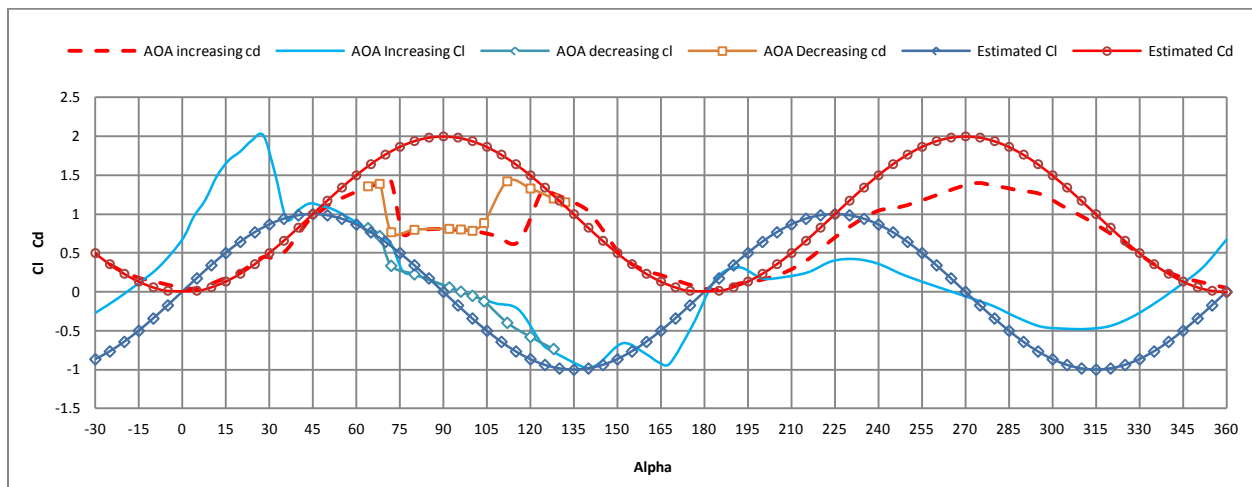


Figure 11: Open test section C_l and C_d (NWT 2005) blade.

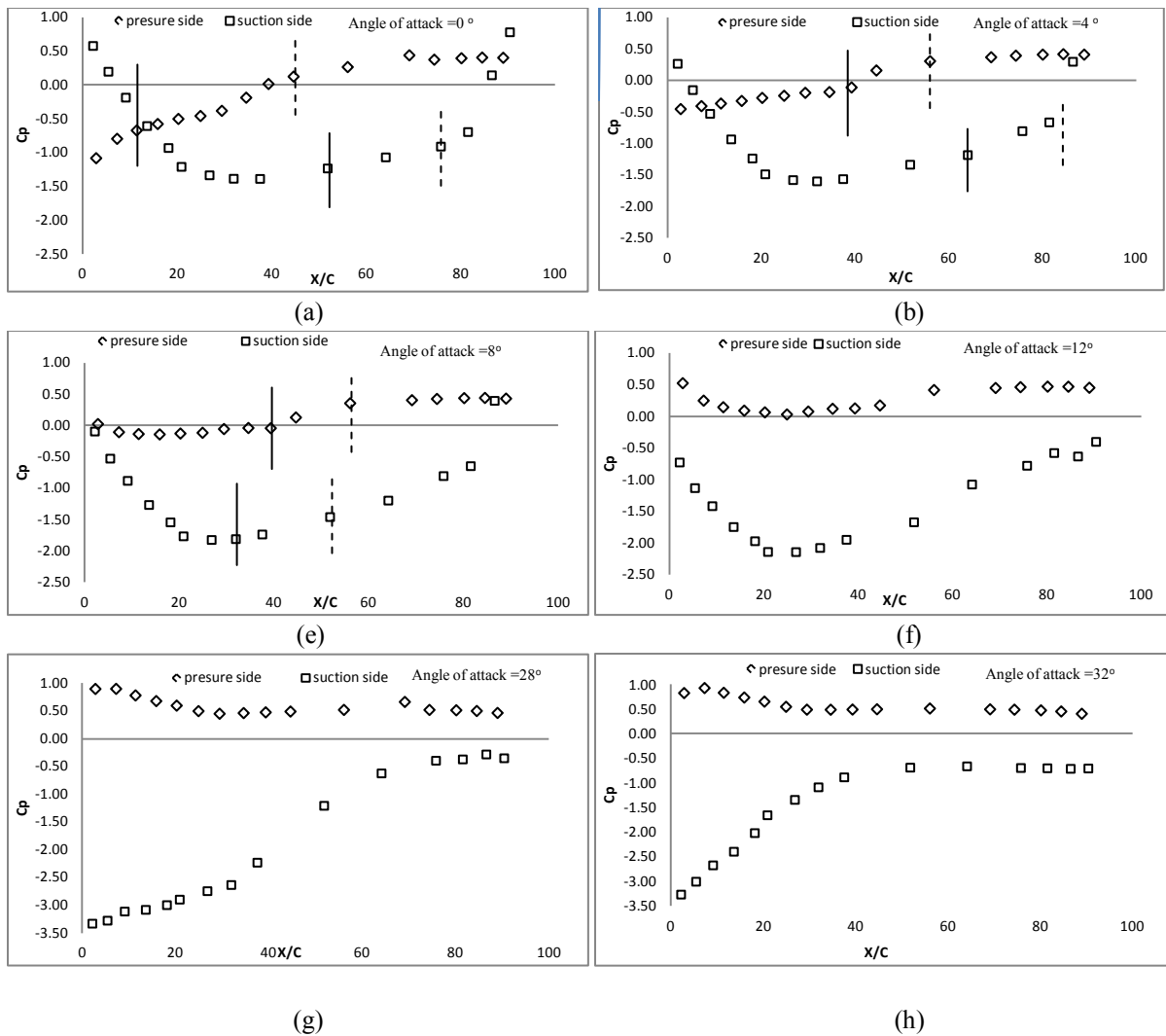
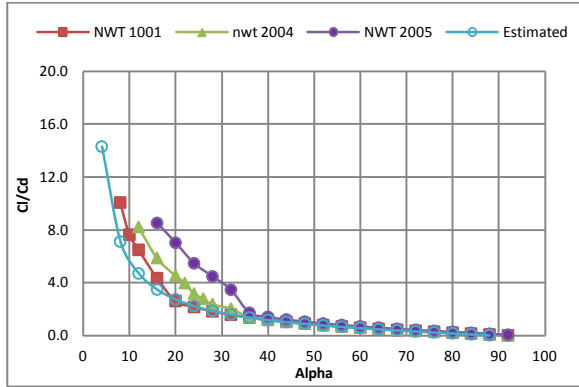


Figure 12: Pressure distribution over the Aerofoil NWT 2005

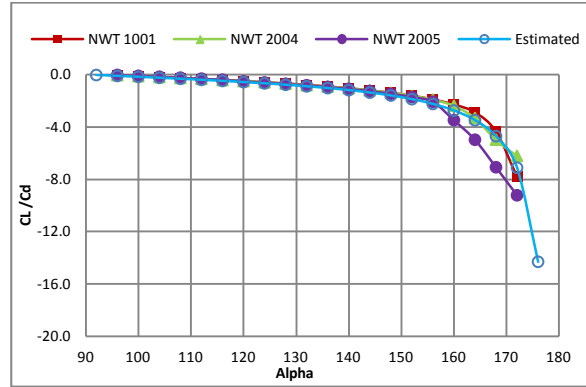
Corresponding to figure 12, it becomes obvious that the separation bubble formed on the pressure side shrinks and moves backwards towards the trailing edge while separation bubbles on the suction side also shrinks in size but it instead moves forward towards the leading edge. These comments seem to be valid for low angles of attack. For higher angle of attack separation bubble bursts leading to stall.

5.1 Lift and Drag at deep-stall angles

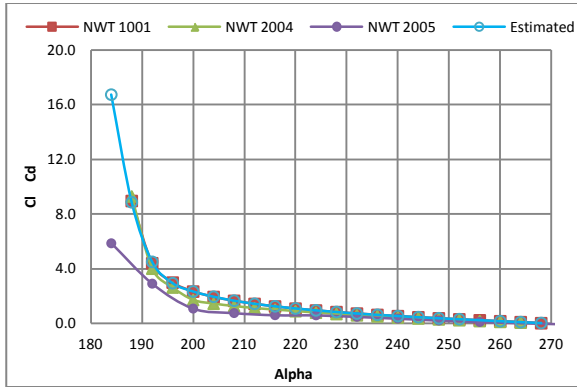
The lift and drag force is based on pressure distribution over an aerofoil with increasing and decreasing angles of attack. The ratio of C_l and C_d is plotted in figure 13 for all angles of attack for all the three aerofoils. For lower angles of attack the C_l over C_d variation is like any other aerofoils. For higher angles of attack around the deep stall region the slope of the C_l over C_d curve is close to 0.025, coinciding with the estimated values using the formulae. This value is same as the one given in reference [6]. At lower angles of attack and also at angles of attack when the trailing edge facing the flow C_l over C_d curves are distinct and different from C_l over C_d curve for the estimated values.



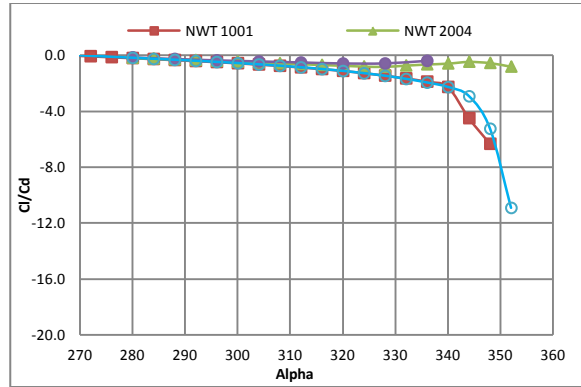
(a)



(b)



(c)



(d)

Figure 13: Ratio of Lift and drag co efficient

6.1 Conclusion:

All the three blades have been experimentally investigated over to 0° to 360° for Reynolds number 2×10^5 . The blades exhibit two stall regions (hard and soft stall) over 0° to 180° and again two stall regions over 180° to 360° deg, the C_l and C_d values in the second region are smaller compared to the first. Stalling angles are 12° , 20° , 28° for the tip, mid and root profiles respectively. While starting of the wind turbine angles of attack varies from 30° to 40° degree in the root to 60° to 80° in the tip regions. Since the C_l values for all the three blades are about 0.6 around these angles of attack, the starting characteristics for the set of blades is good. When operating at the design point, ratio of lift and drag values are kept high giving the design power extraction from the wind turbine. Stall hysteresis for all the three blades are located at deep stall regions and hence will not affect the starting and design point performance of the wind turbine. These blades are not suitable for VAWT machines since they exhibit stall hysteresis.

Commercial CFD codes with proper attention to Reynolds number range and mildly separated flows can be used to predict the performance of airfoils up to the stall regime. This can be extended up to the complex three dimensional flows in an actual wind turbine unless the flow

detachment is not too large. For large angle of attack computations CFD is not a good tool to be relied upon. Instead we can opt for numerical curve fit methods which are available in literature for angles of attack after stall regime. With the use of these two tools combined together one can design a better wind turbine with a good starting and operating characteristics.

7.1 References:

1. **Wilson, R.** and **Lissaman, P.** *Applied aerodynamics of wind power machines*, 1974 (State University, Oregon).
2. **Wilson, R. Lissaman, P.,** and **Walker, S.** *Aerodynamic performance of wind turbines*, 1976 (State University, Oregon).
3. **McCarty, J.** *PROP93 Users guide*, (Alternative Energy Institute).
4. **Worasinchai, S. Ingram, G** and **Dominy, R.** *A low Reynolds-member, High-angle- of attack investigation of wind turbine aerofoils*, 2011(Durham University, UK).
5. **Daniel J. Walter** *Study of Aerofoils at High Angle of Attack, in Ground Effect*, school of aerospace, mechanical & manufacturing engineering Portfolio of science, engineering & technology Rmit university September 2007
6. W.A. Timmer , *Aerodynamic characteristics of wind turbine blade airfoils at high angles-of-attack*, Delft University of Technology Faculty of Aerospace Engineering Kluyverweg 1, 2629 HS Delft, The Netherlands.

Appendix I

1. Cp plot for variable angles attack without Confined flow NWT 1001

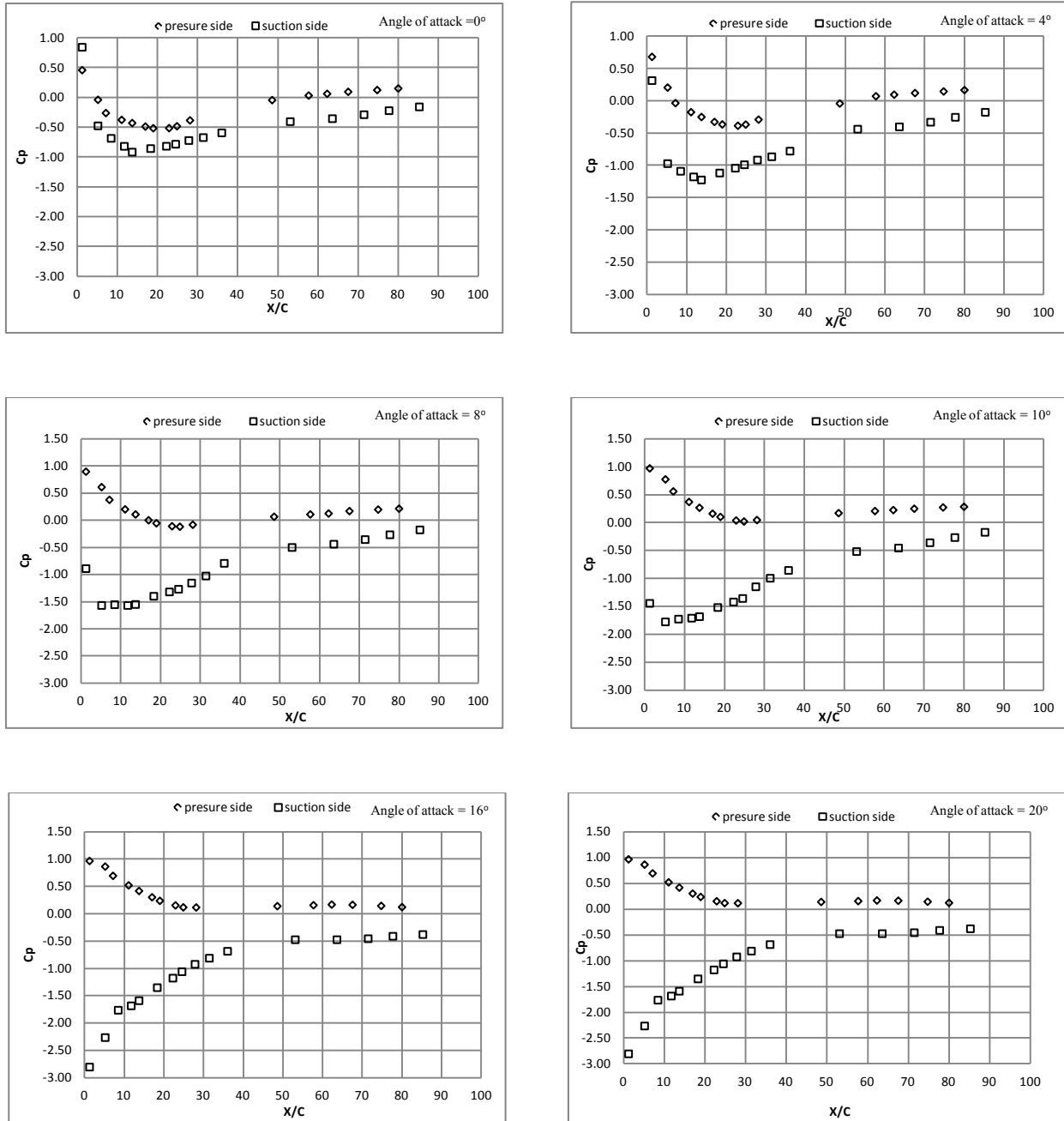


Figure 14(a): Pressure Distribution over the airfoil for angles of attack from 0 to 20 degree

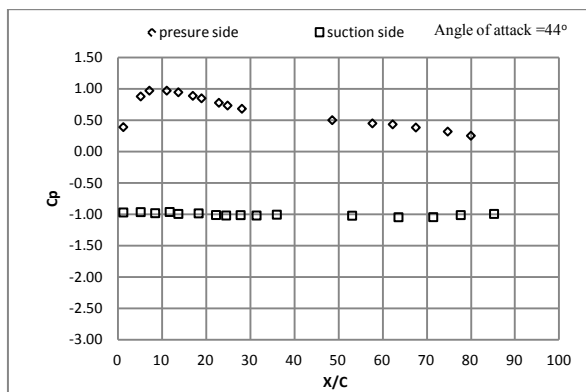
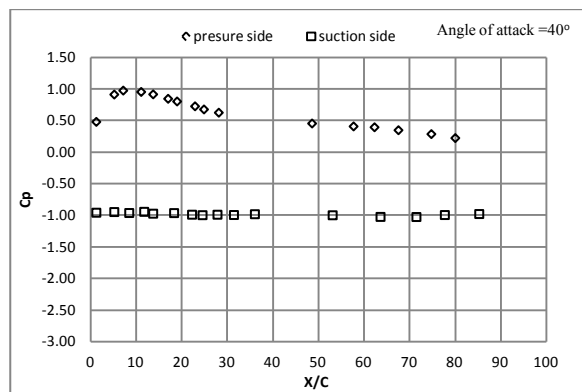
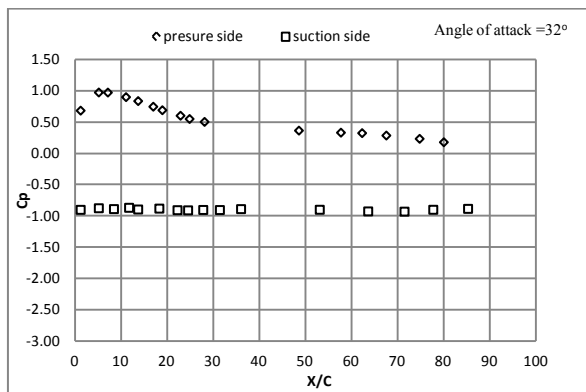
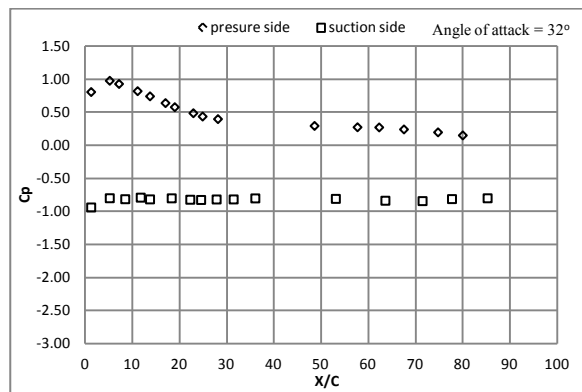
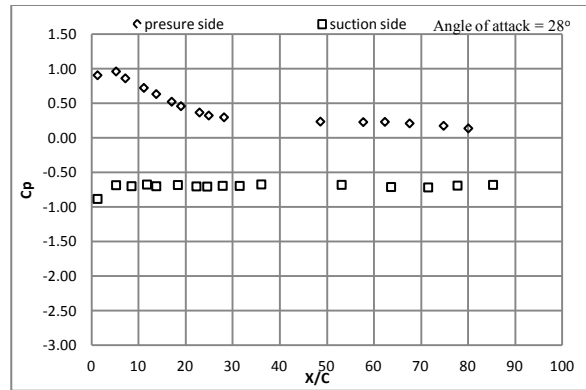
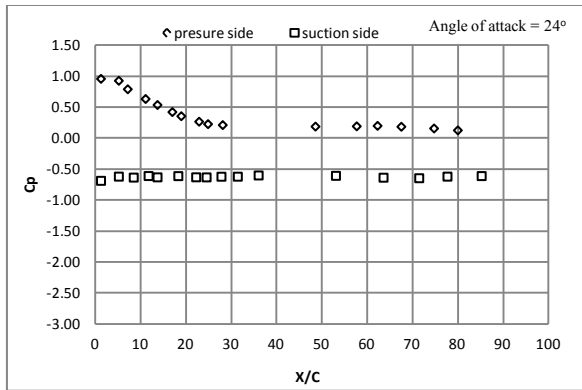


Figure 14(b): Pressure Distribution over the airfoil for angles of attack from 24 to 44 degree

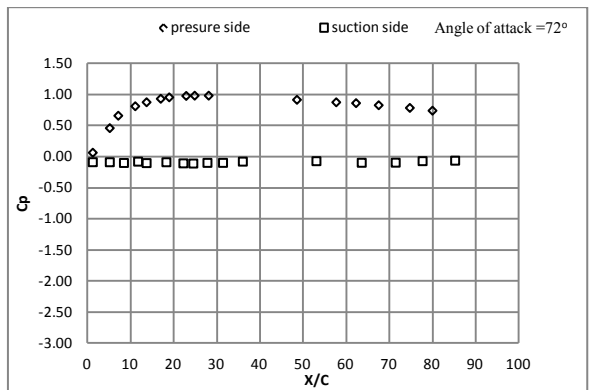
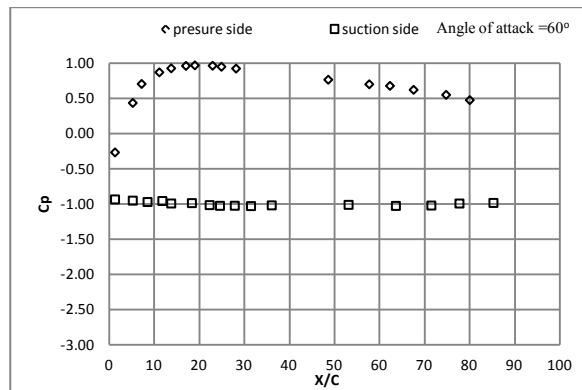
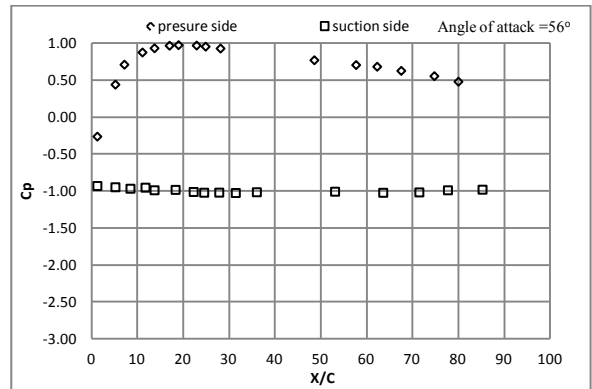
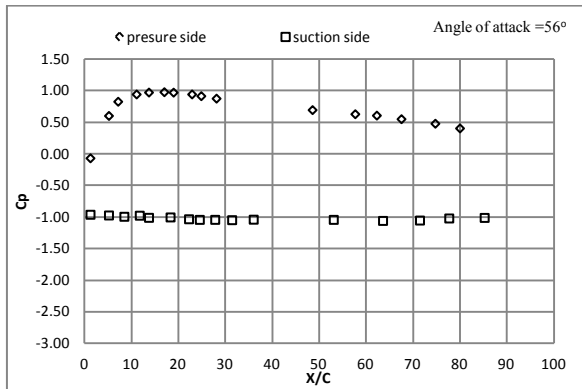
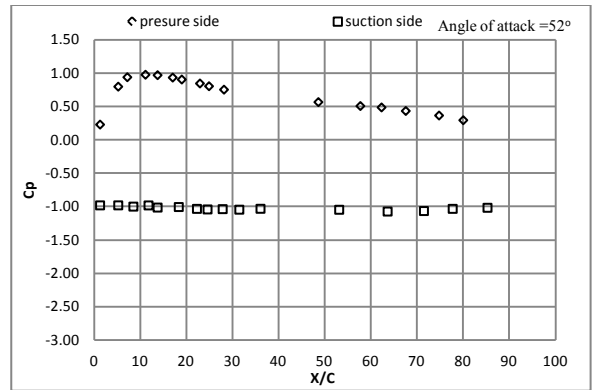
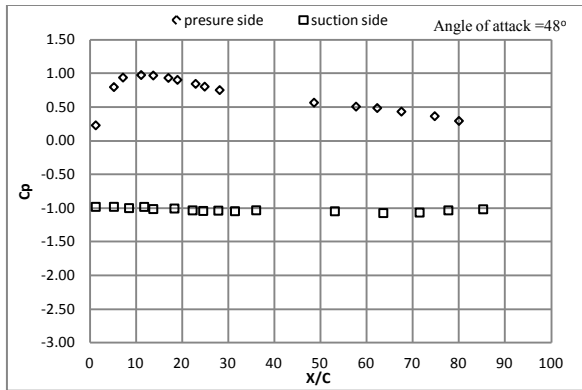


Figure 14(c): Pressure Distribution over the aerofoil for angles of attack from 48 to 72 degree

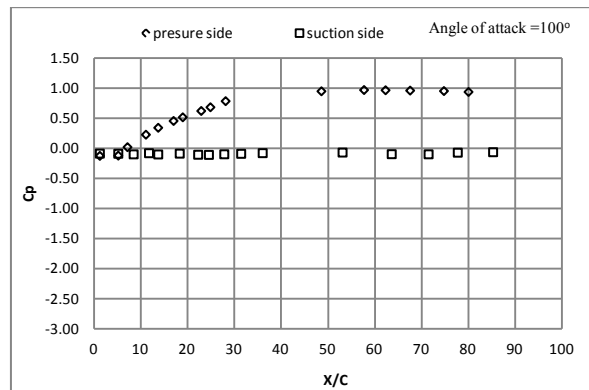
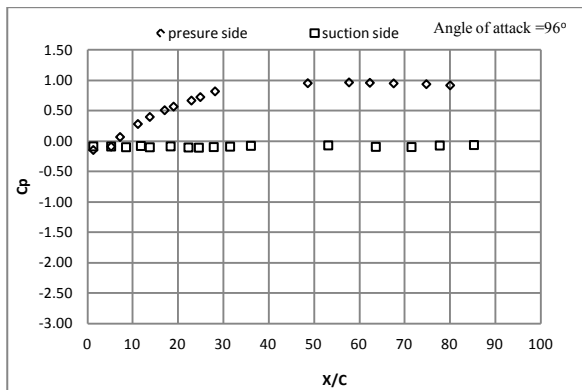
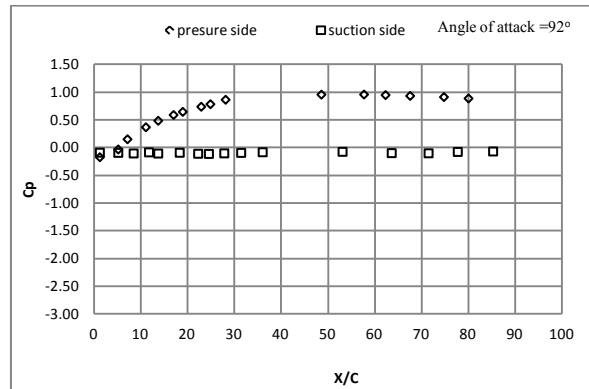
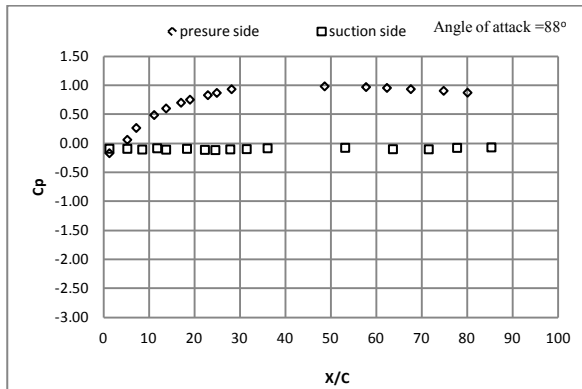
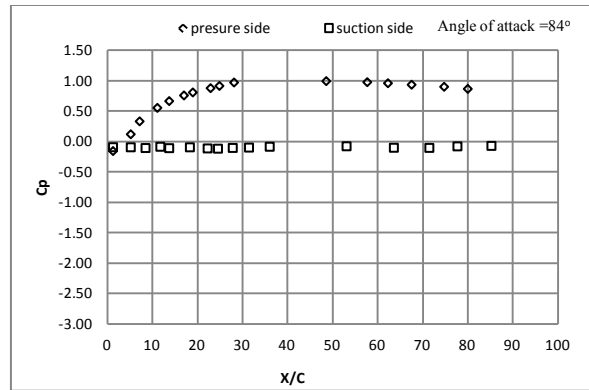
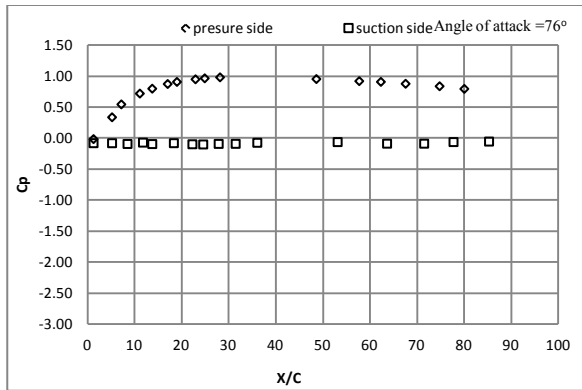


Figure 14(d): Pressure Distribution over the aerofoil for angles of attack from 76 to 100 degree

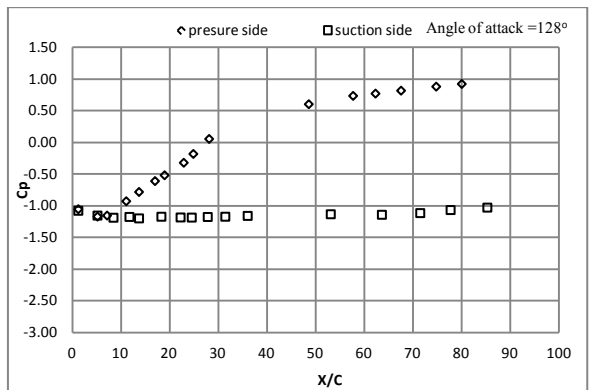
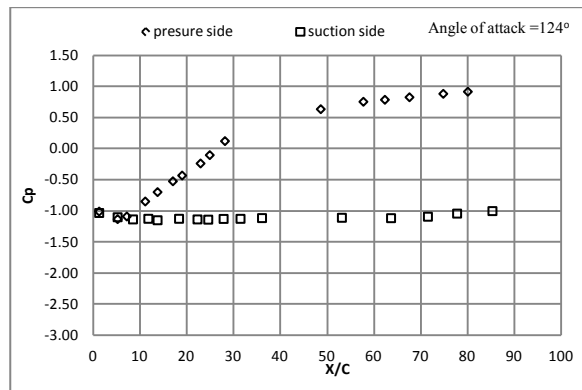
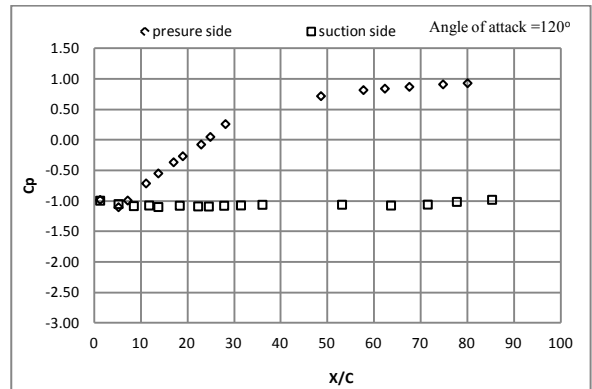
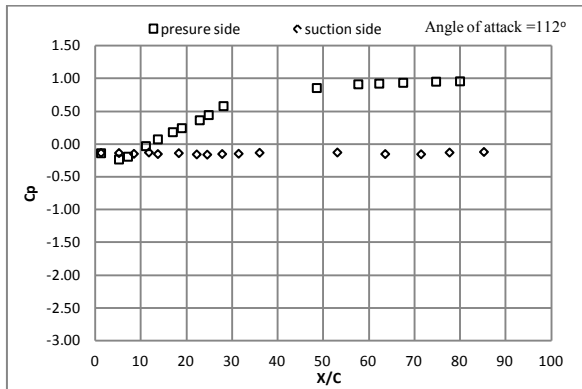
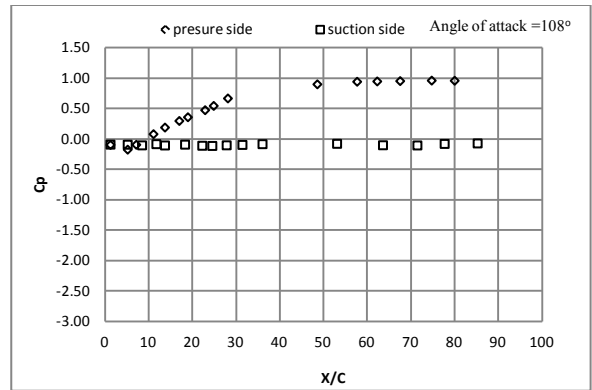
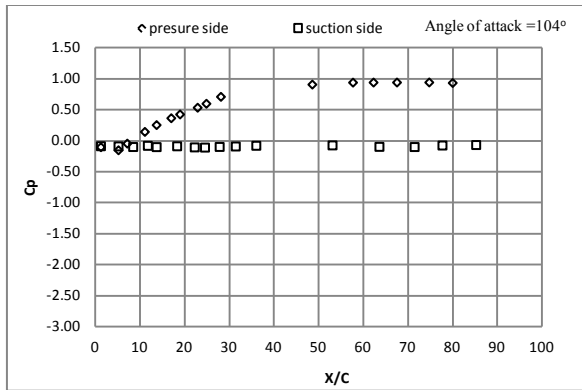


Figure 14(e): Pressure Distribution over the aerofoil for angles of attack from 104 to 128 degree

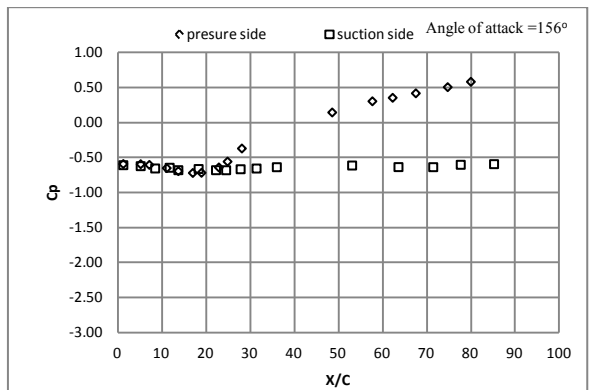
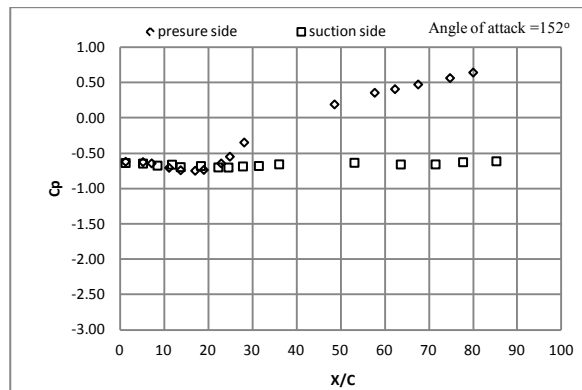
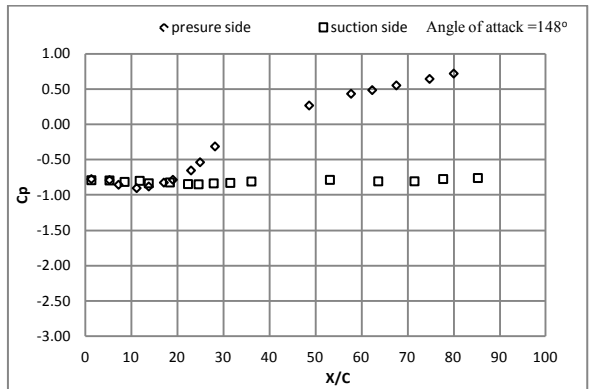
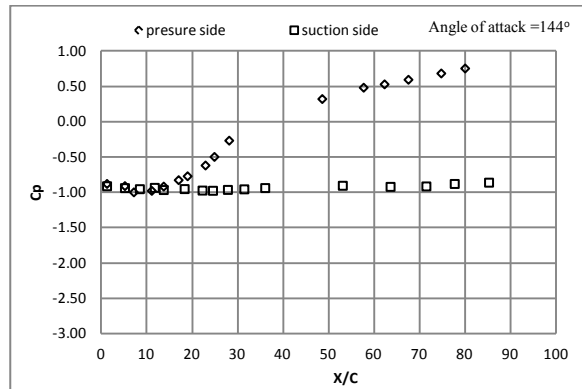
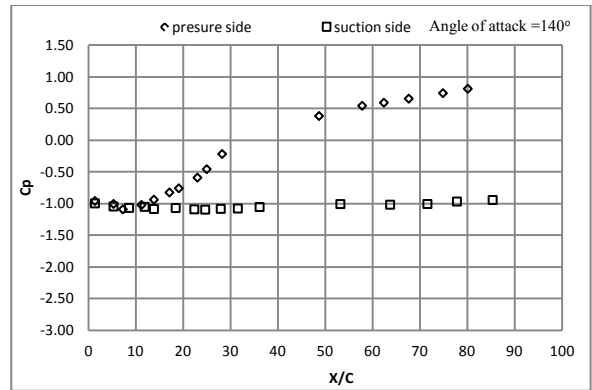
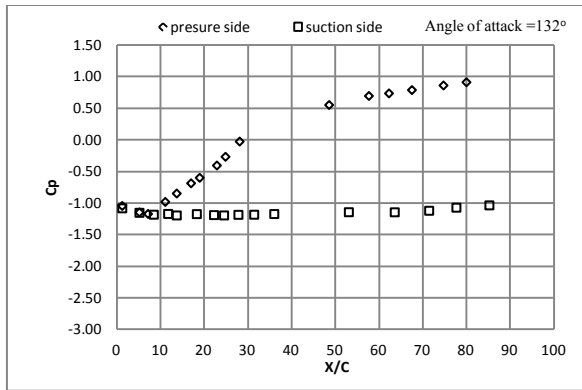


Figure 14(f): Pressure Distribution over the aerofoil for angles of attack from 132 to 156 degree

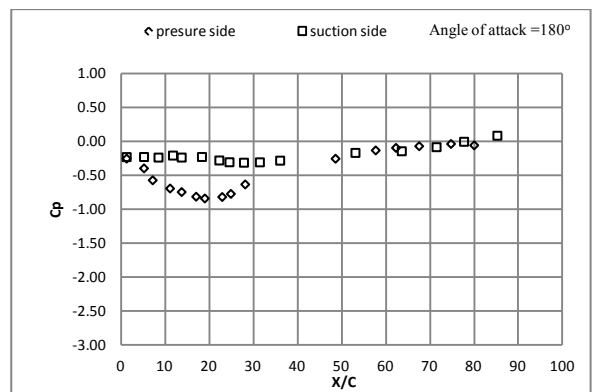
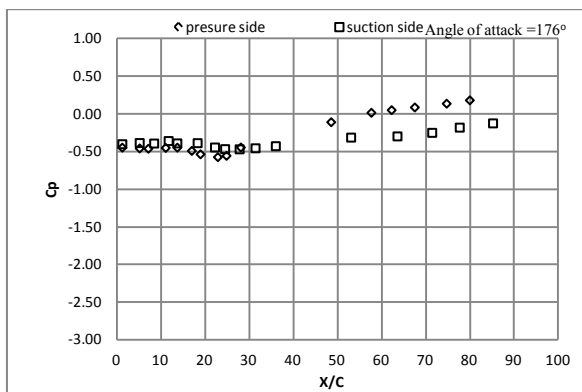
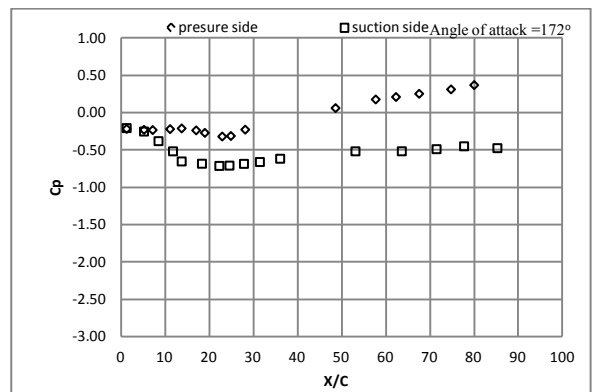
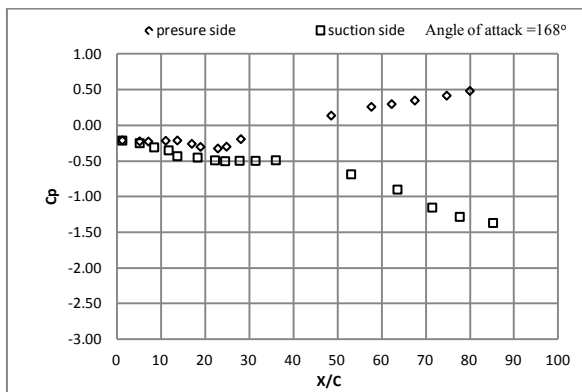
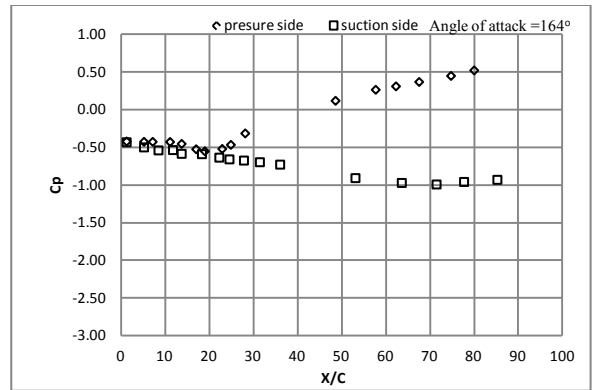
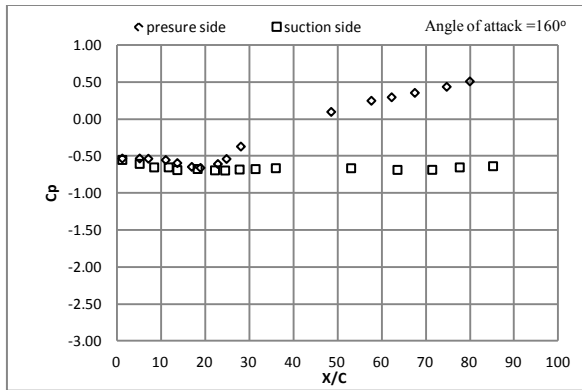


Figure 14(g): Pressure Distribution over the aerofoil for angles of attack from 160 to 180 degree

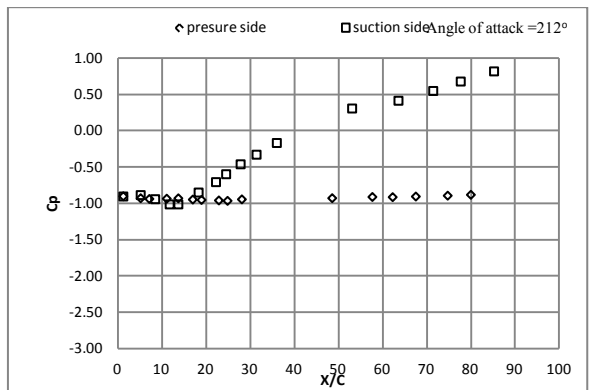
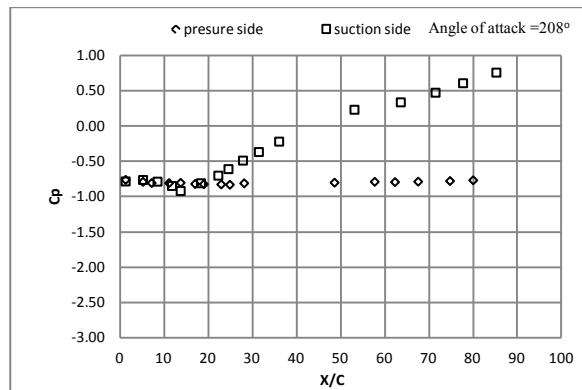
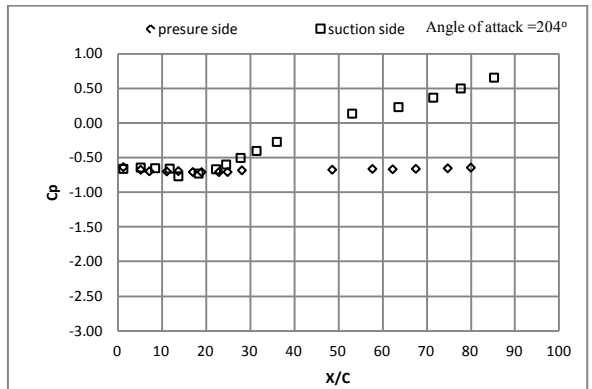
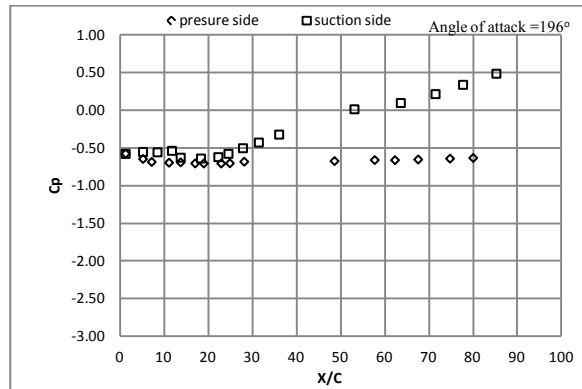
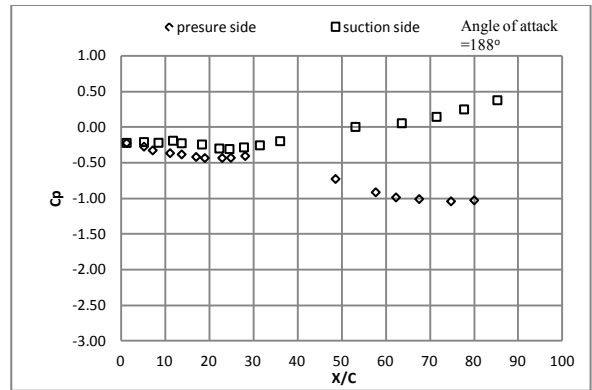
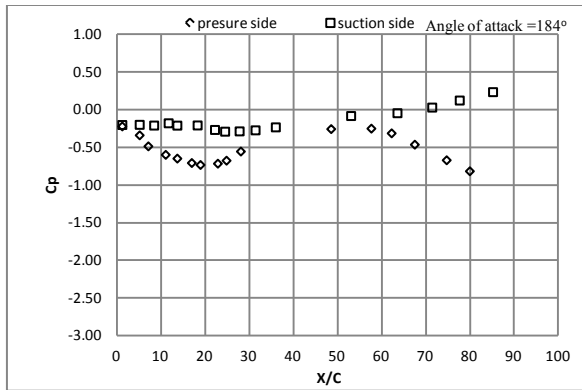


Figure 14(h): Pressure Distribution over the aerofoil for angles of attack from 184 to 212 degree

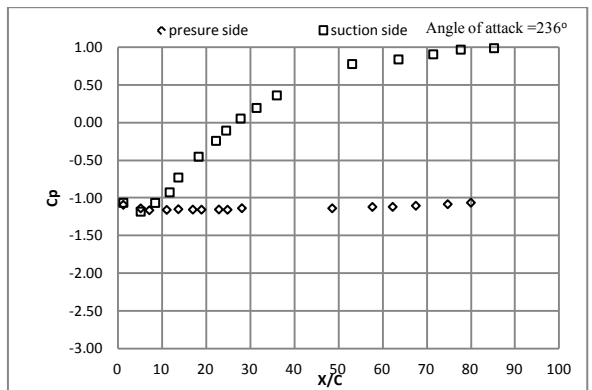
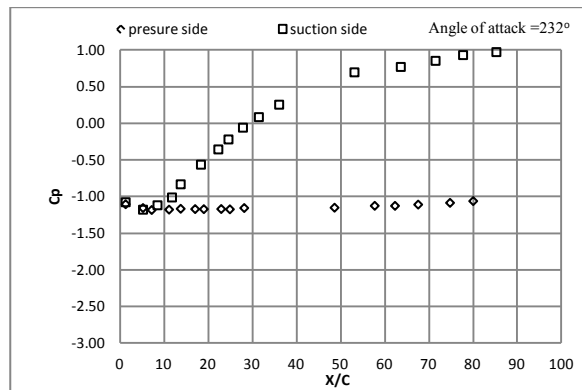
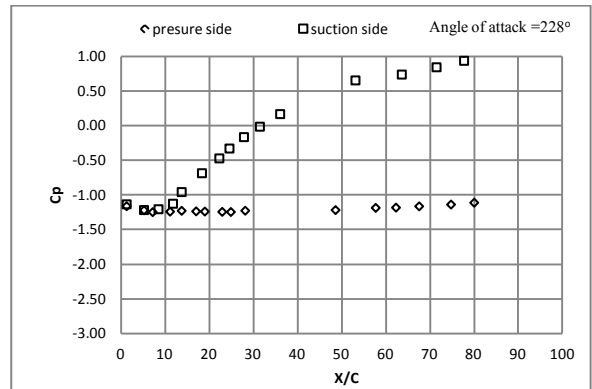
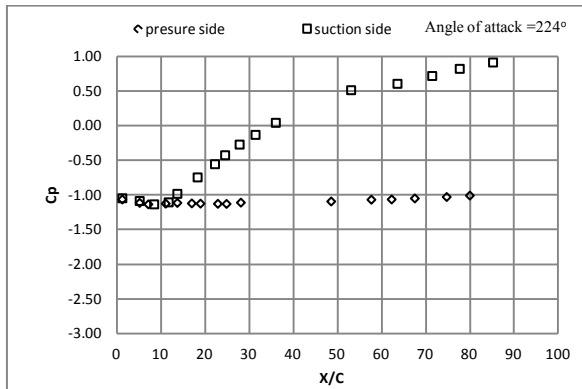
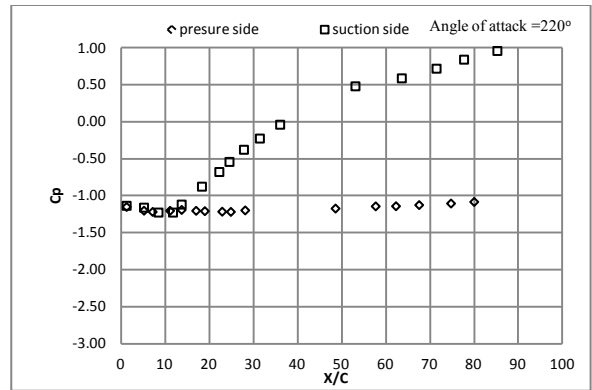
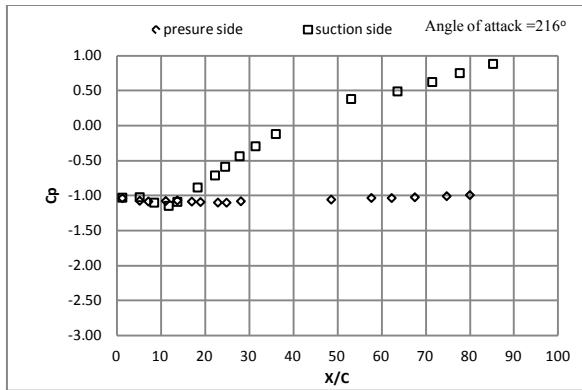


Figure 14(i): Pressure Distribution over the aerofoil for angles of attack from 216 to 236 degree

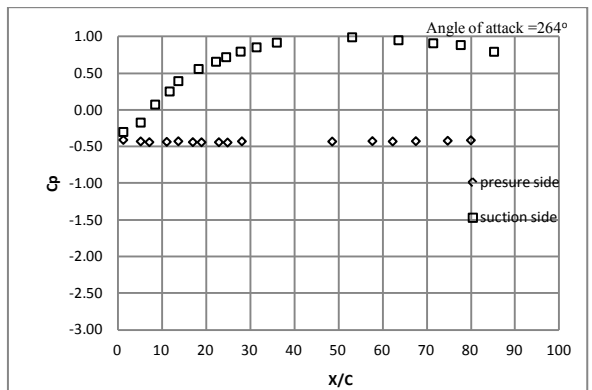
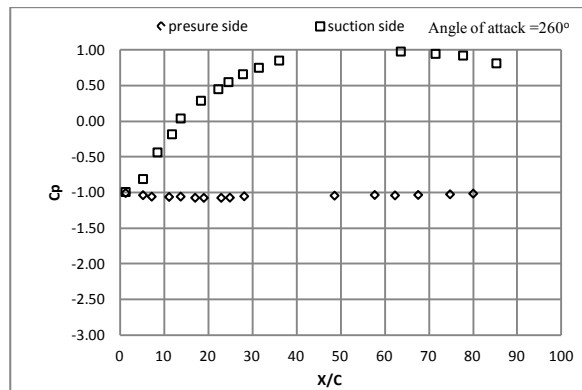
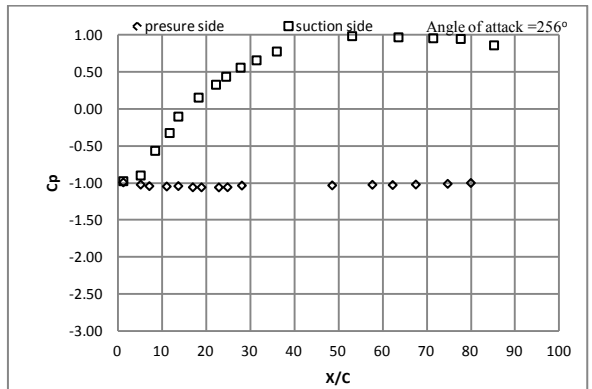
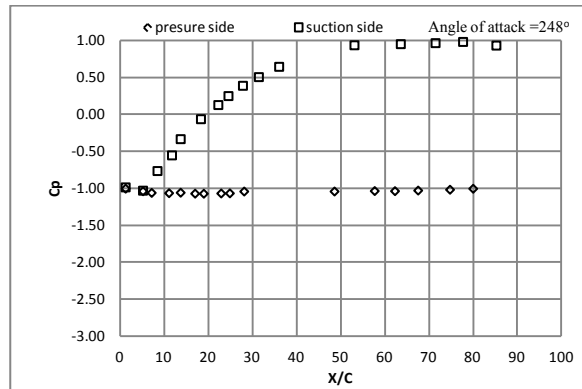
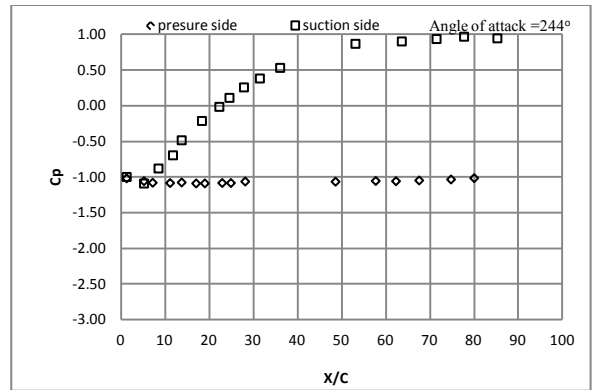
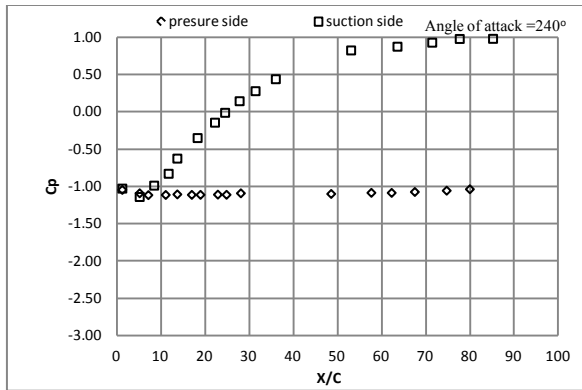


Figure 14(j): Pressure Distribution over the aerofoil for angles of attack from 240 to 264 degree

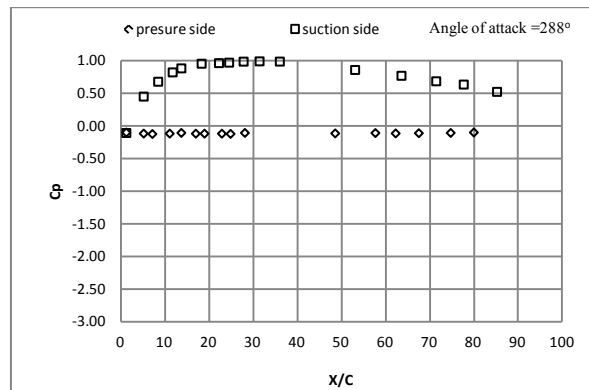
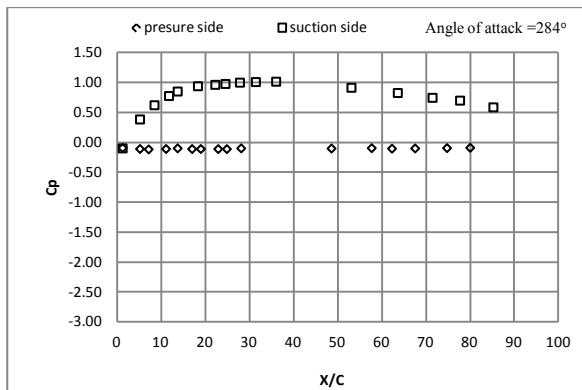
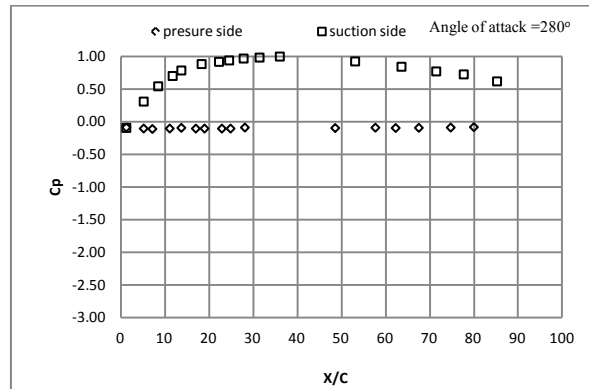
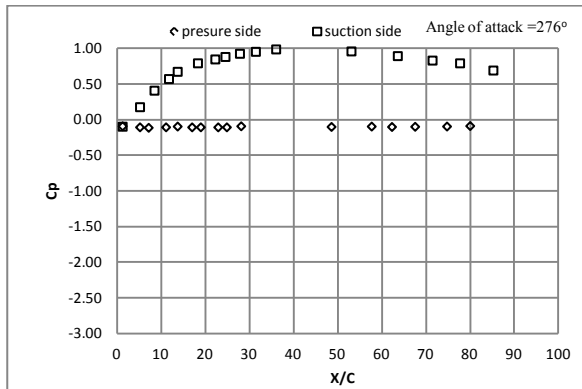
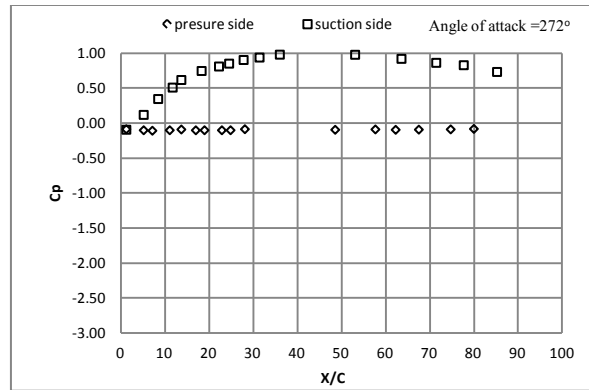
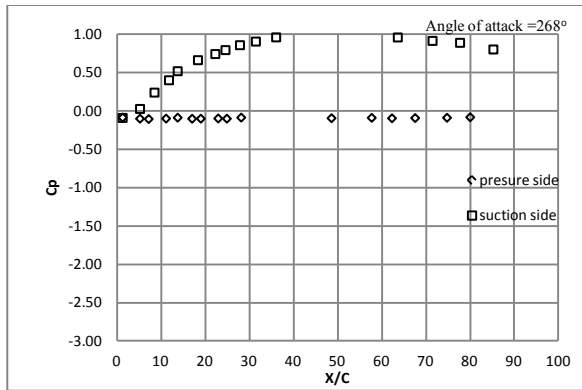


Figure 14(k): Pressure Distribution over the aerofoil for angles of attack from 268 to 288 degree

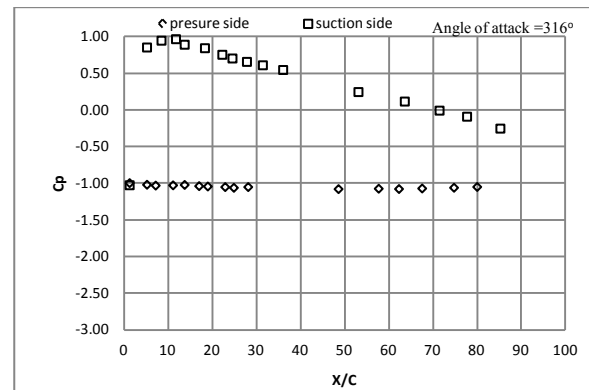
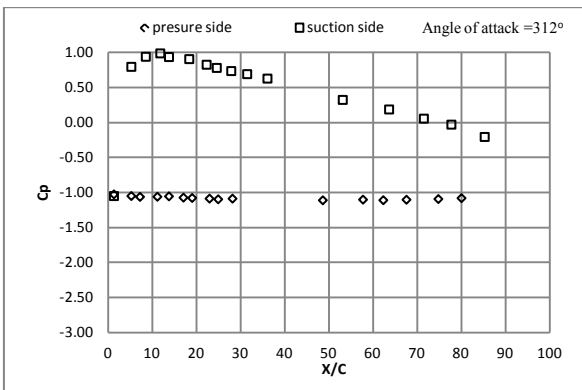
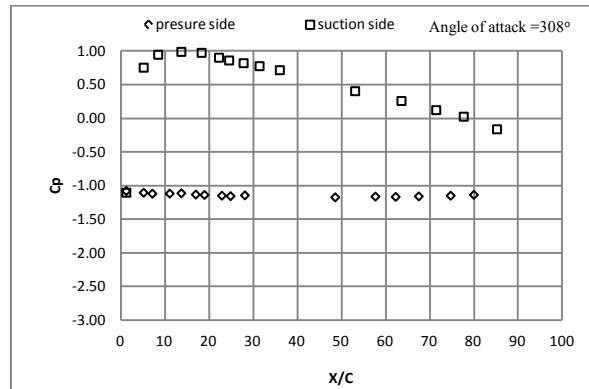
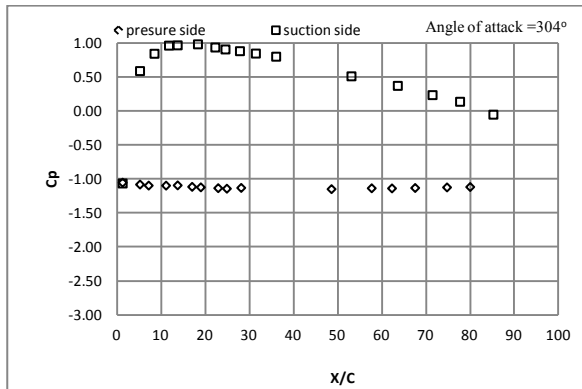
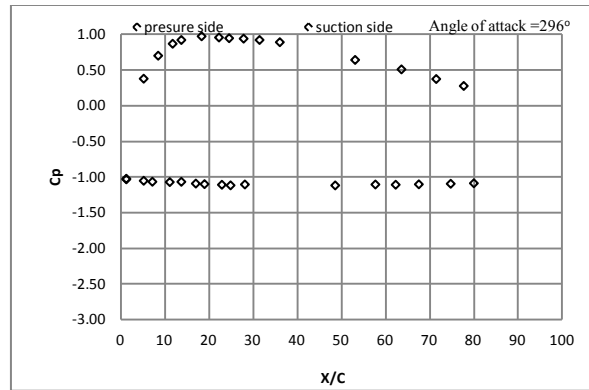
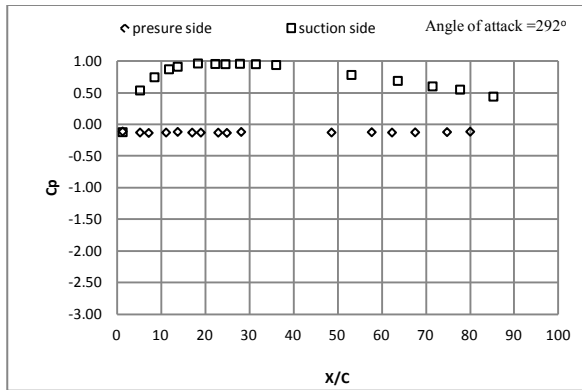


Figure 14(l): Pressure Distribution over the aerofoil for angles of attack from 292 to 316 degree

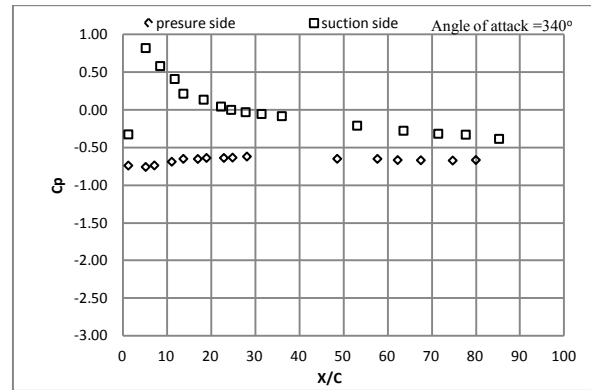
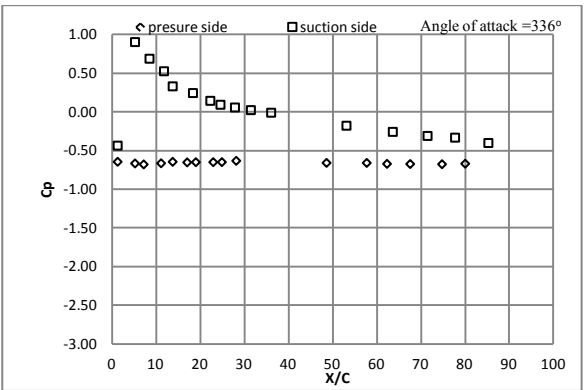
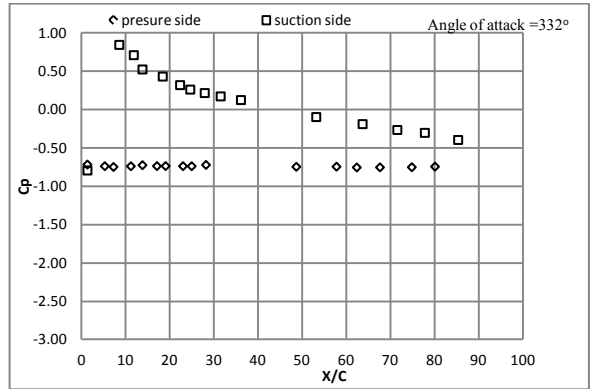
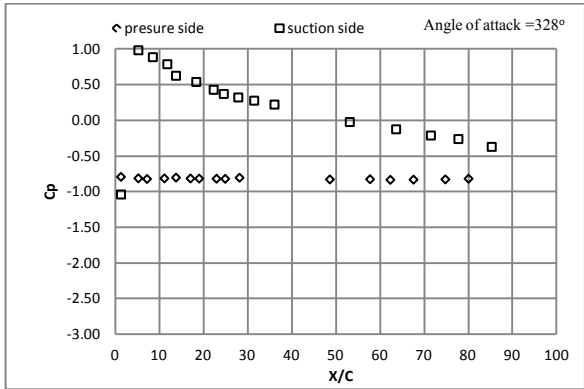
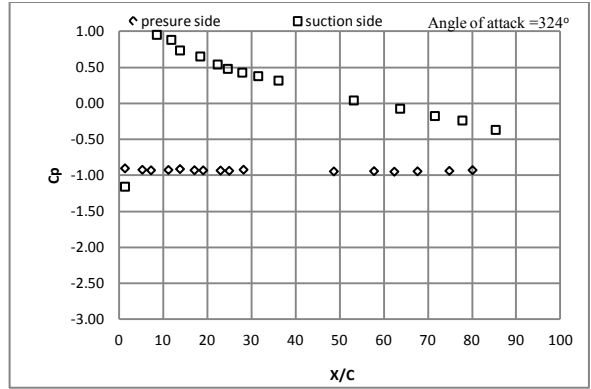
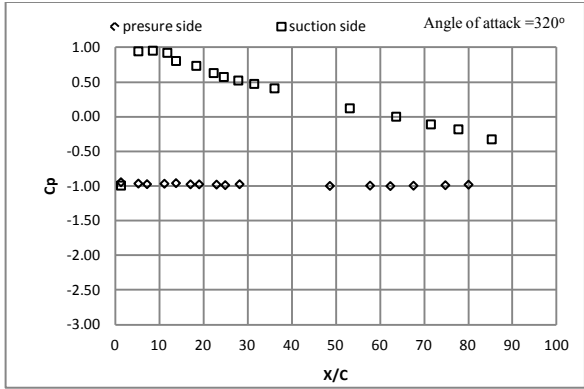


Figure 14(m): Pressure Distribution over the aerofoil for angles of attack from 320 to 340 degree

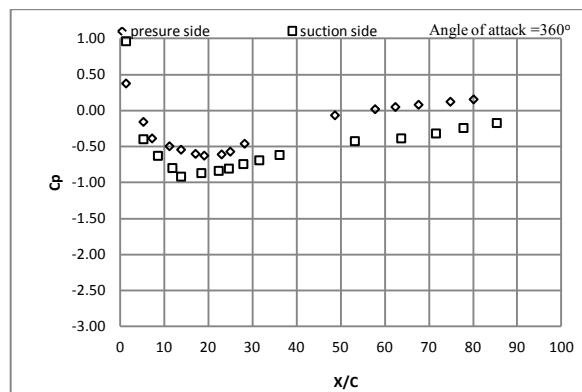
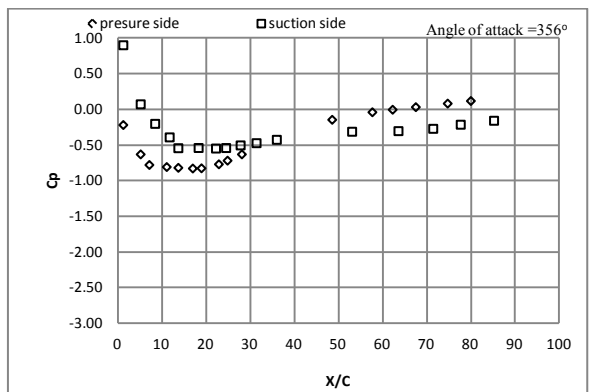
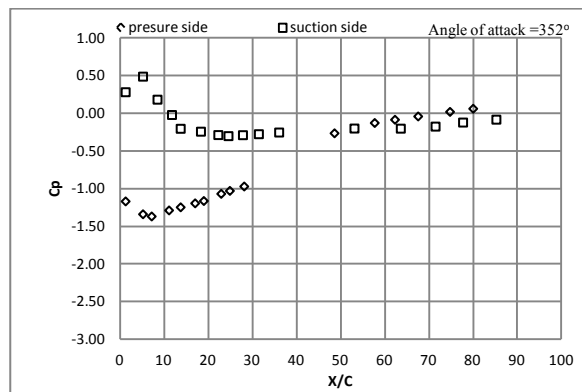
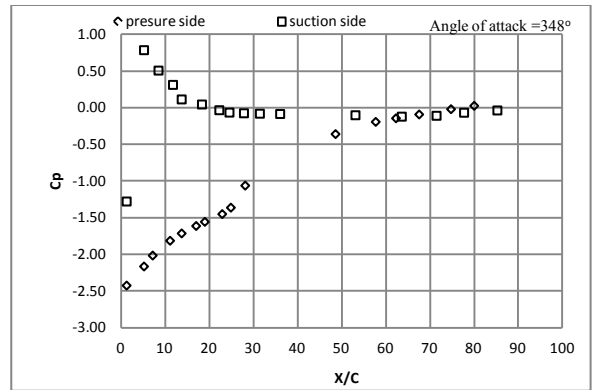
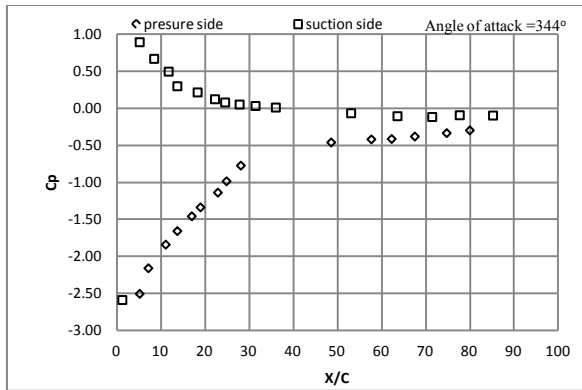


Figure 14(n): Pressure Distribution over the aerofoil for angles of attack from 334 to 360 degree

2. Cp plot for variable angles of attack NWT 2004

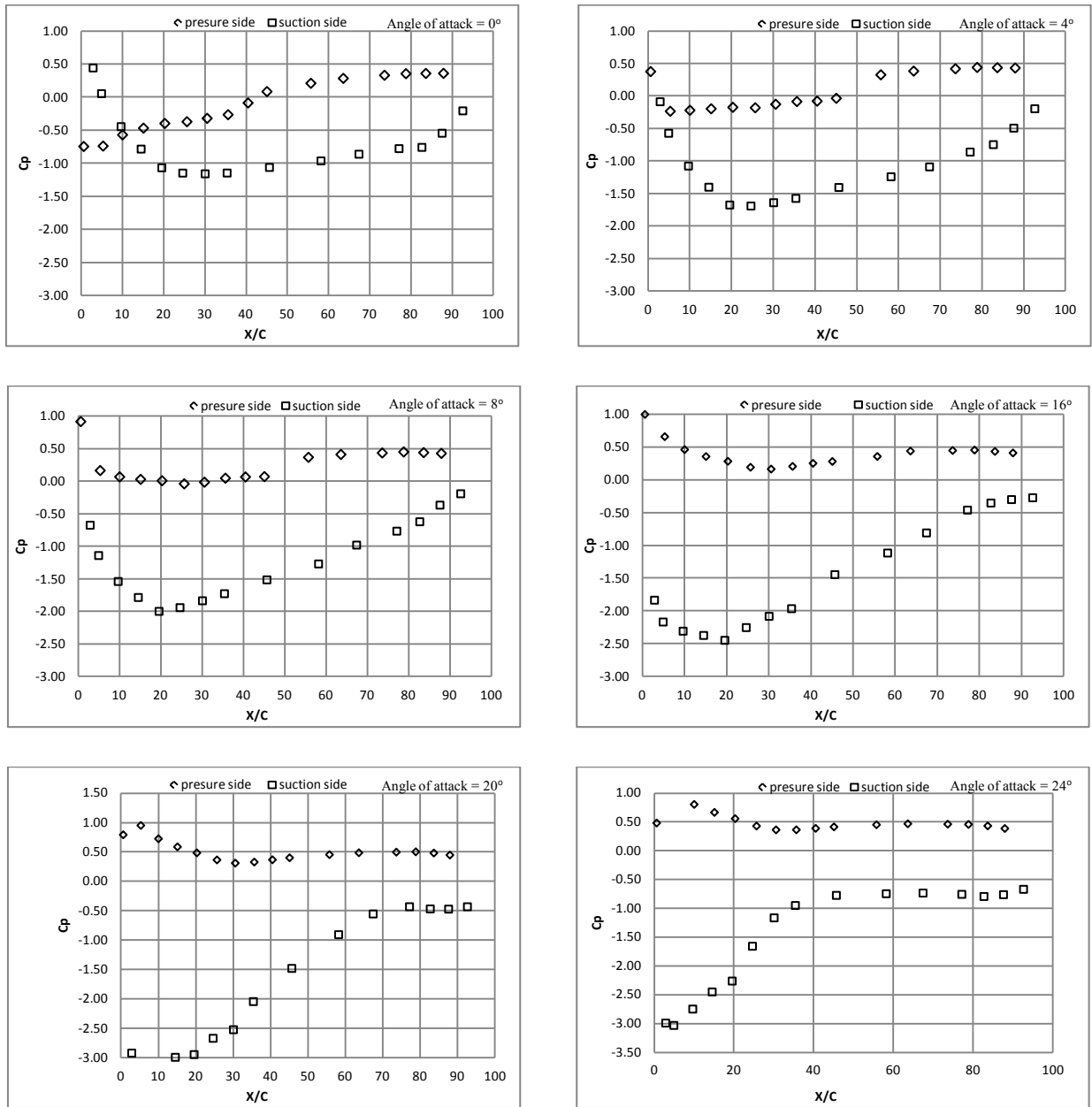


Figure 15(a): Pressure Distribution over the aerofoil for angles of attack from 0 to 20 degree

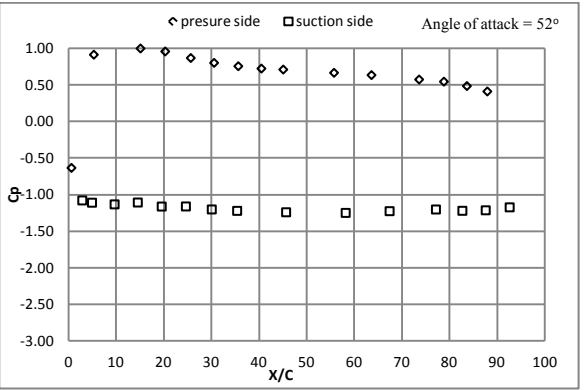
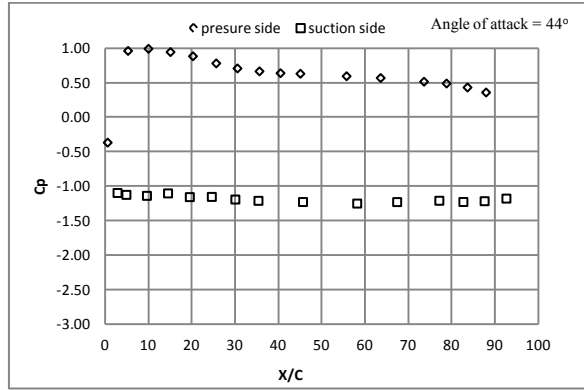
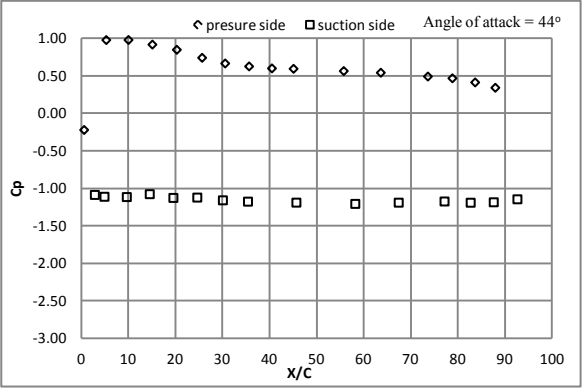
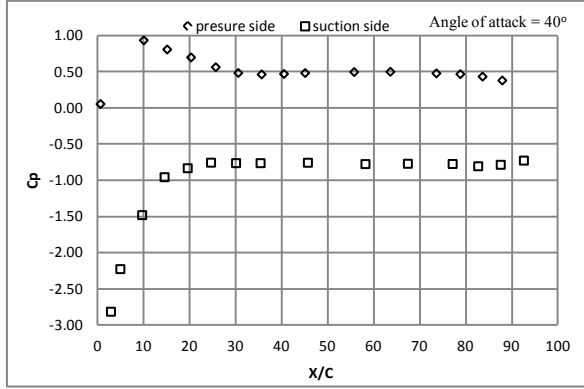
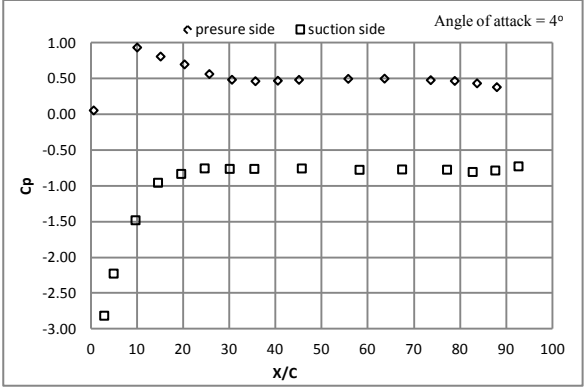
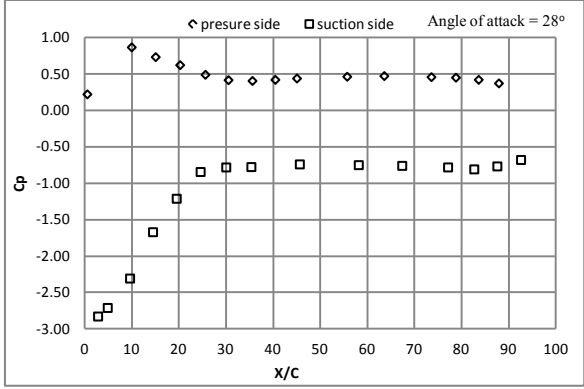


Figure 15(b): Pressure Distribution over the aerofoil for angles of attack from 28 to 52 degree

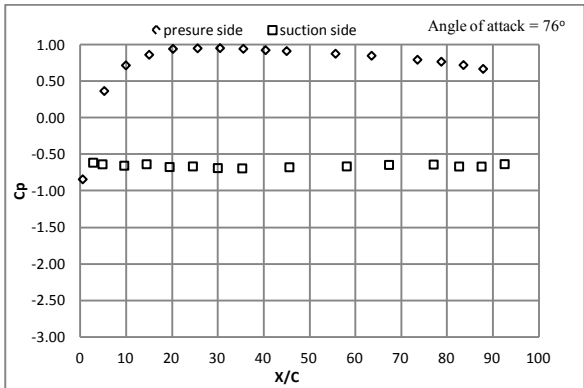
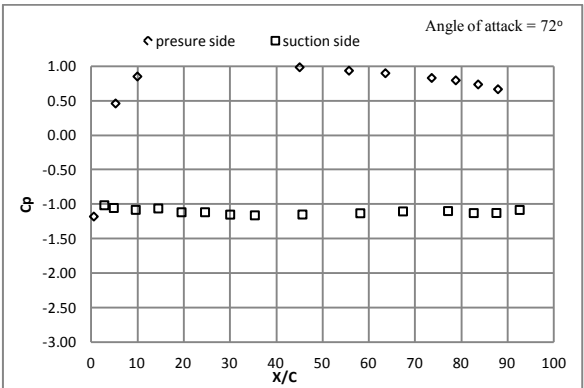
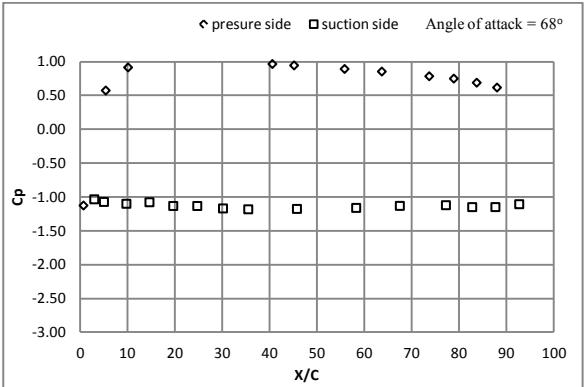
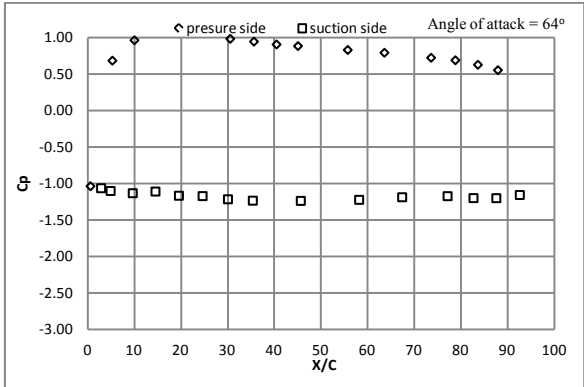
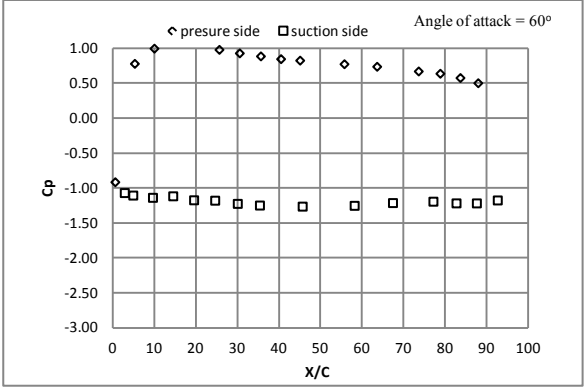
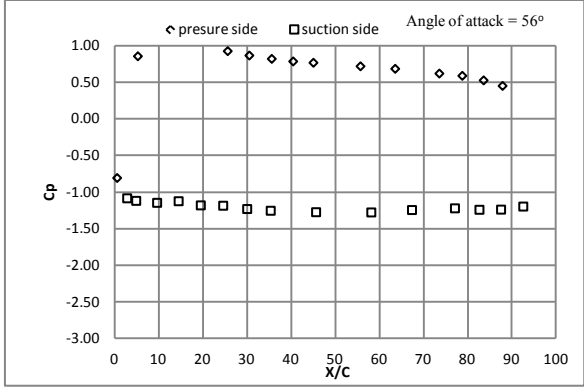


Figure 15(c): Pressure Distribution over the aerofoil for angles of attack from 56 to 76 degree

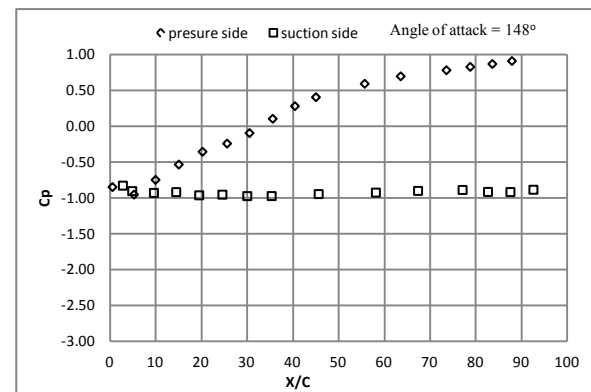
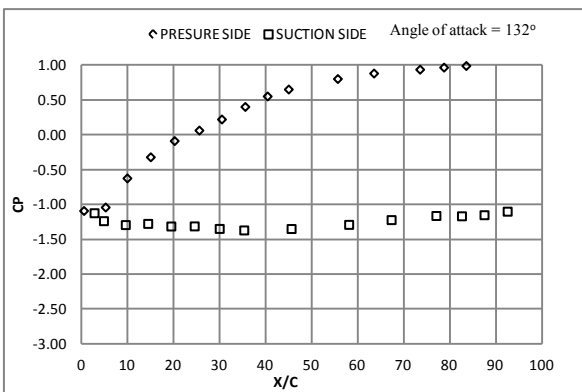
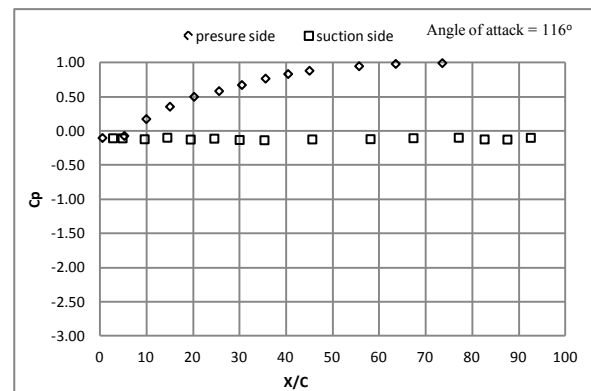
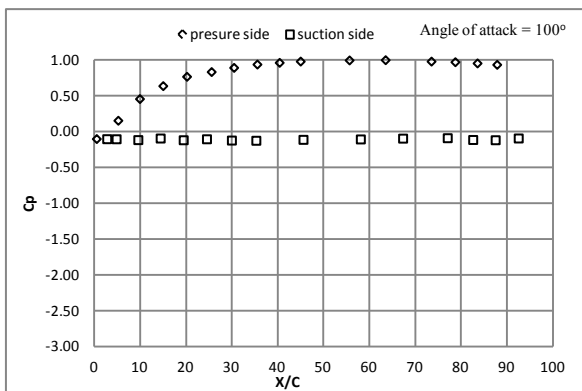
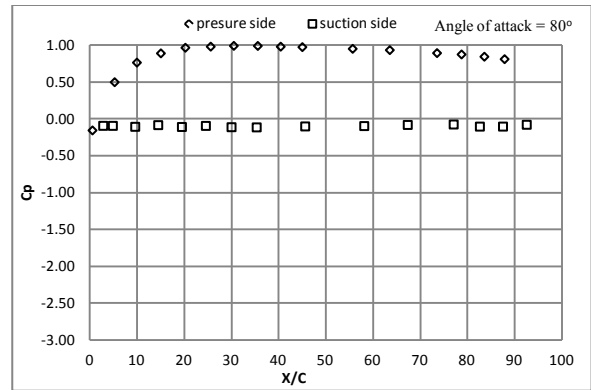
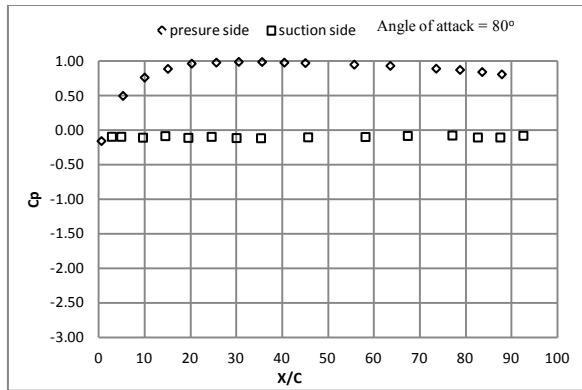


Figure 15(d): Pressure Distribution over the aerofoil for angles of attack from 80 to 148 degree

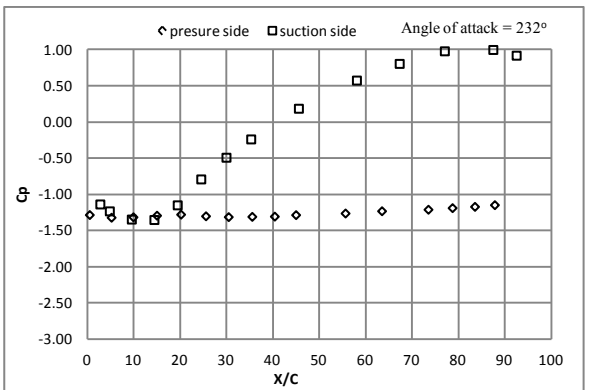
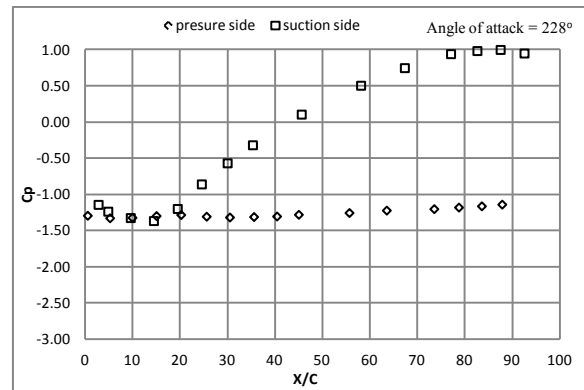
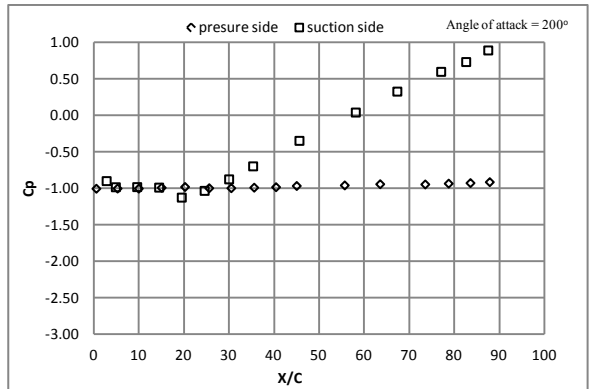
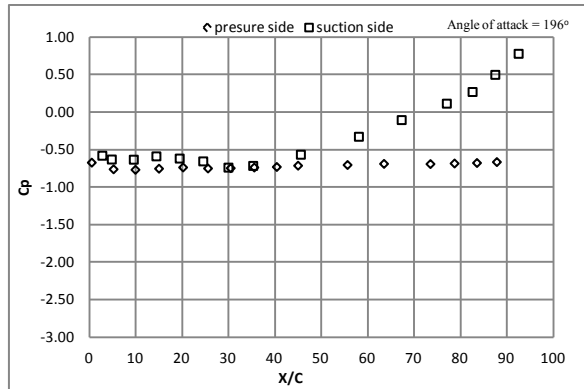
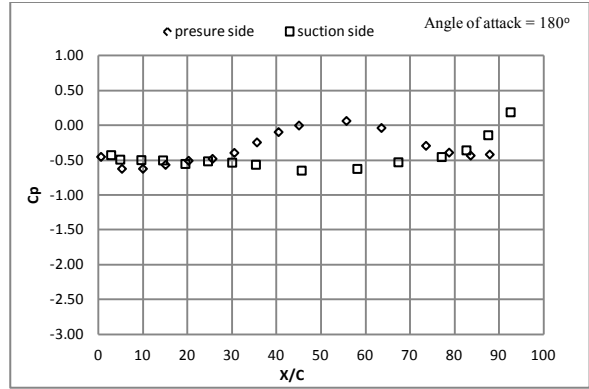
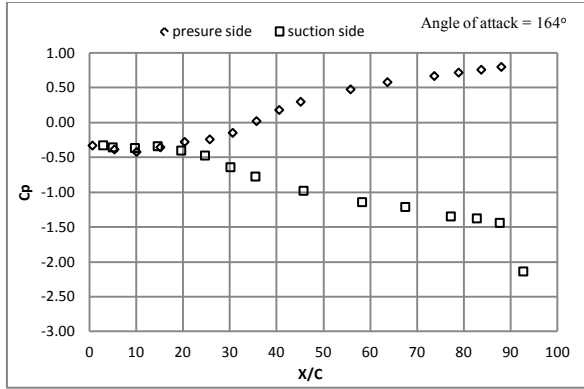


Figure 15(e): Pressure Distribution over the aerofoil for angles of attack from 164 to 232 degree

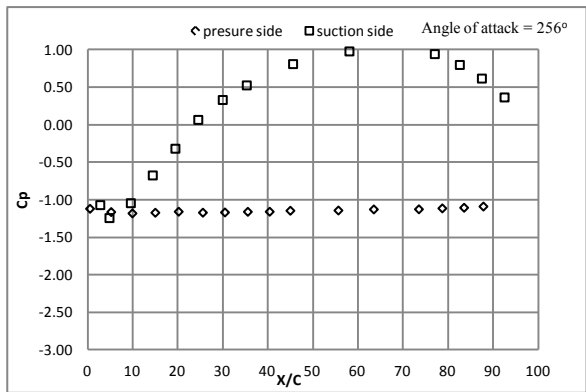
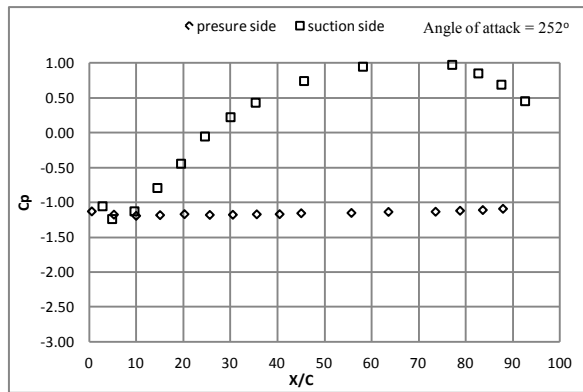
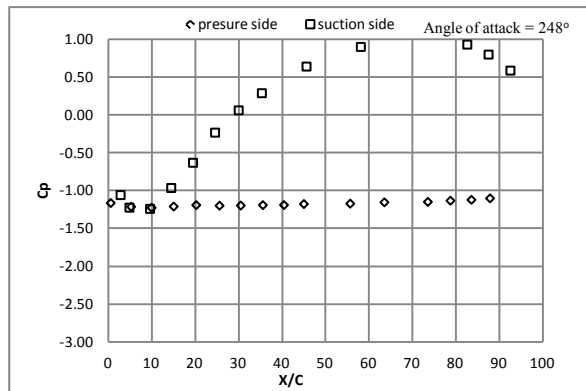
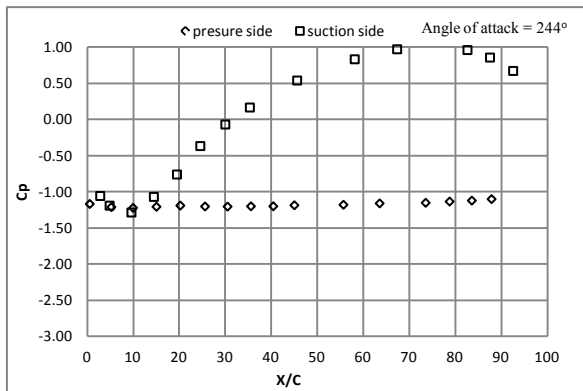
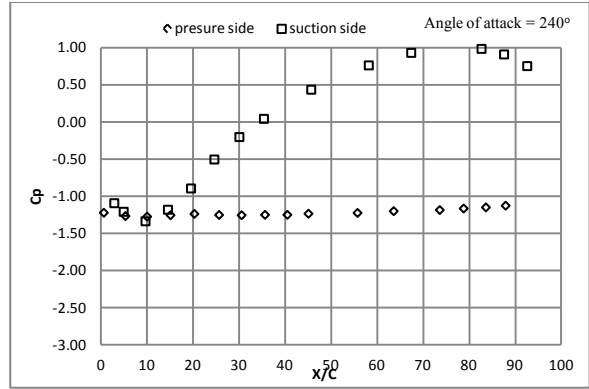
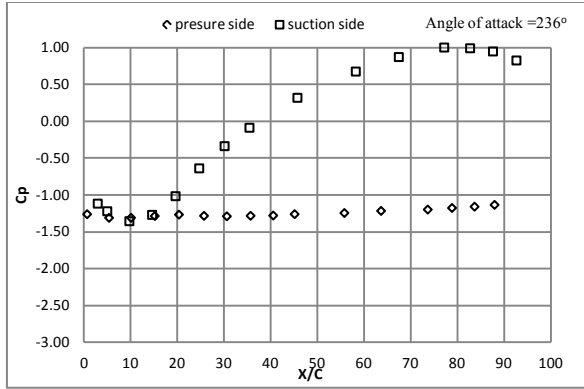


Figure 15(f): Pressure Distribution over the aerofoil for angles of attack from 236 to 256 degree

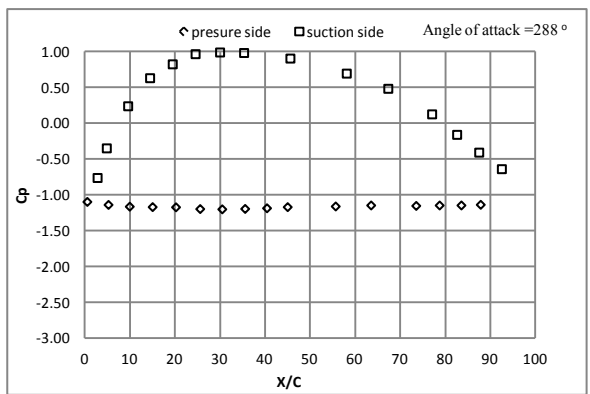
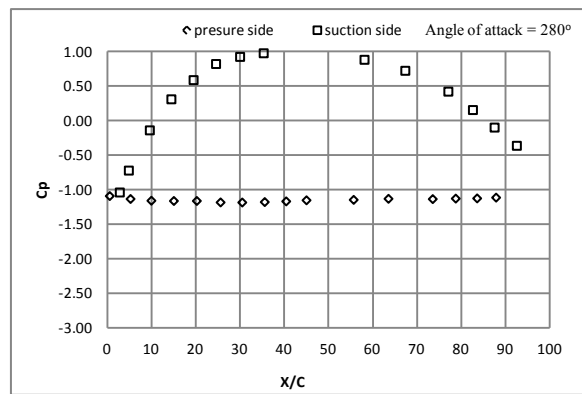
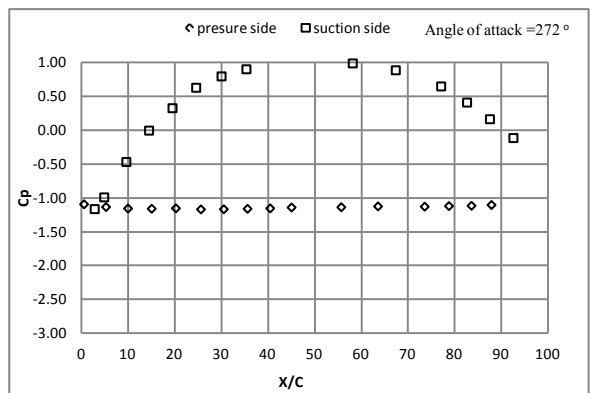
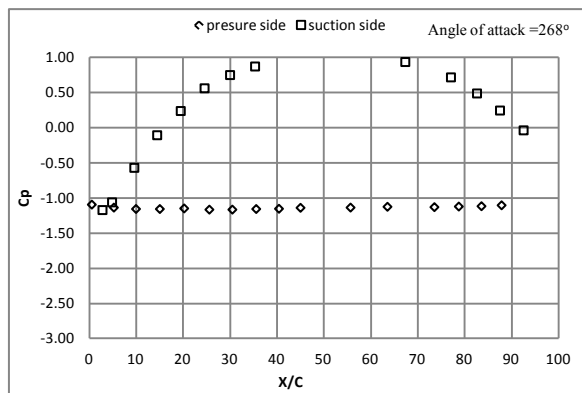
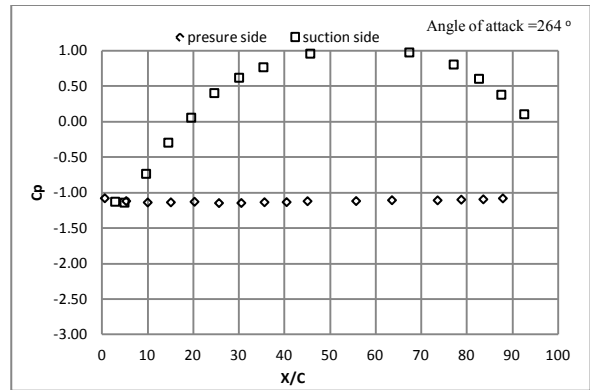
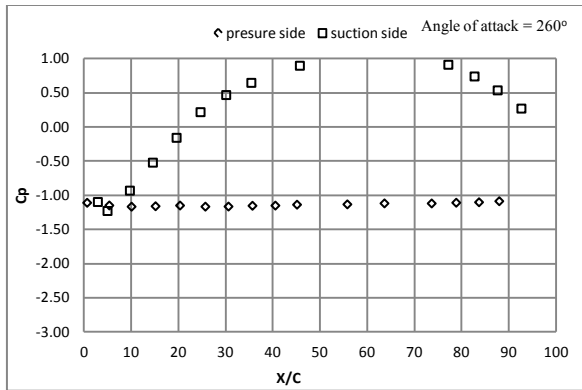


Figure 15(g): Pressure Distribution over the aerofoil for angles of attack from 260 to 288 degree

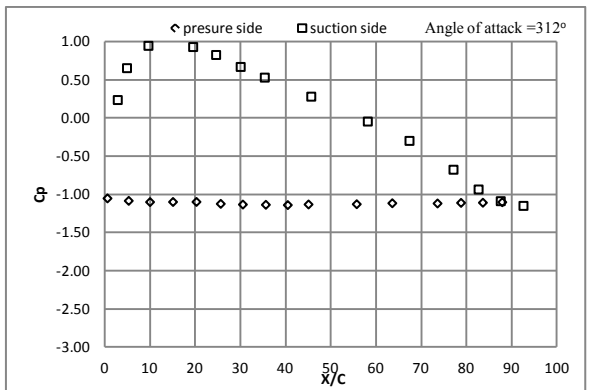
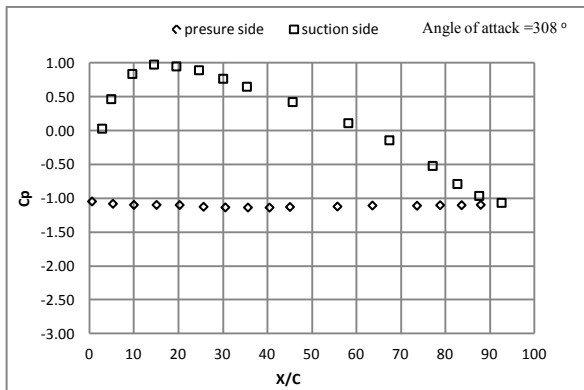
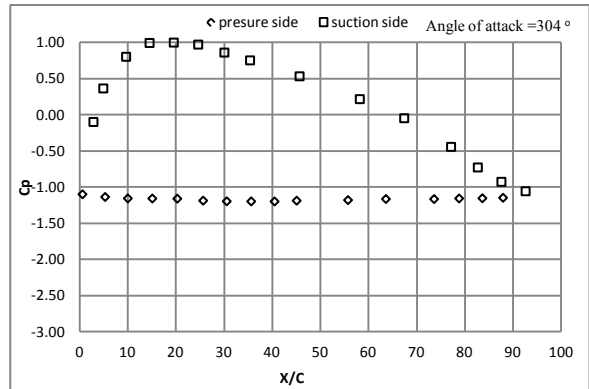
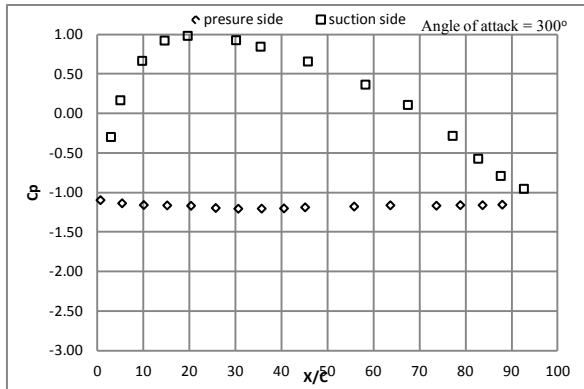
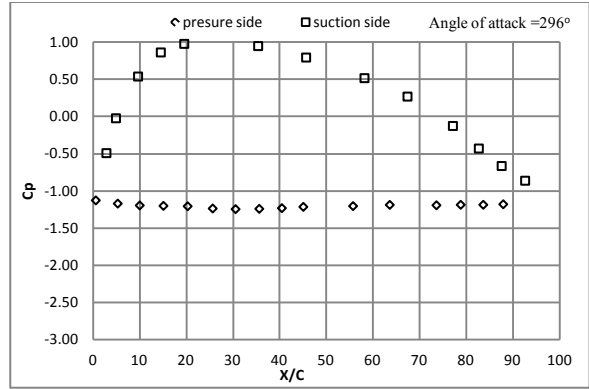
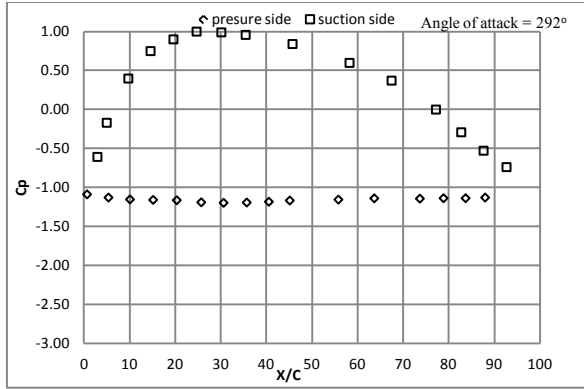


Figure 15(h): Pressure Distribution over the aerofoil for angles of attack from 292 to 312 degree

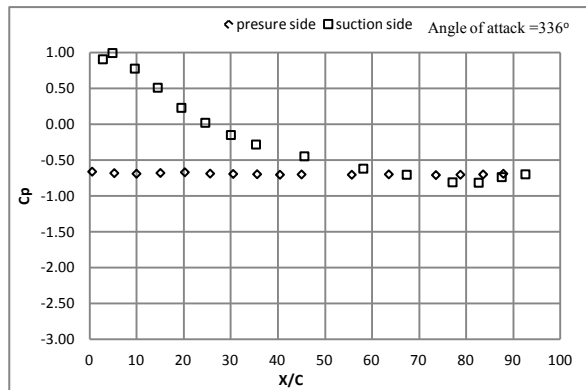
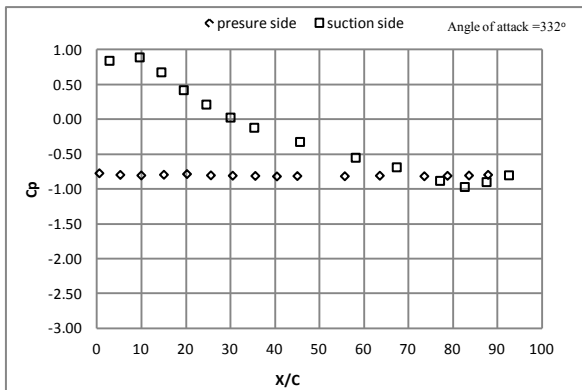
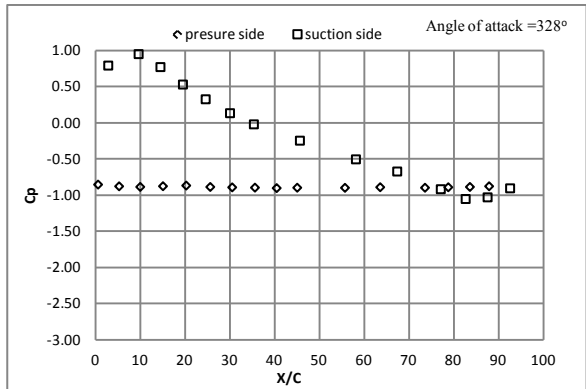
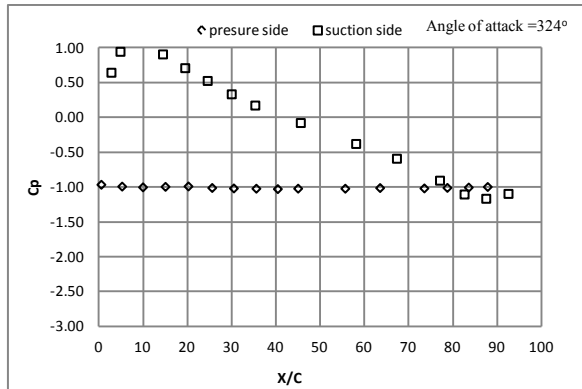
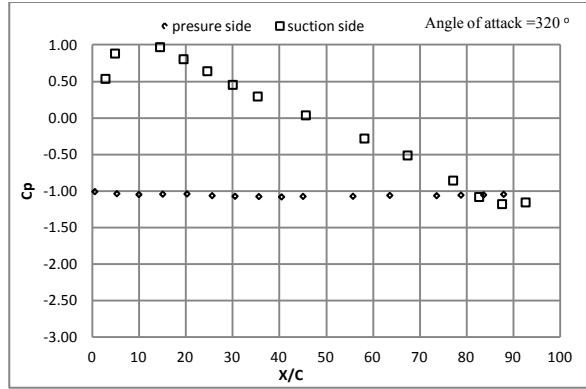
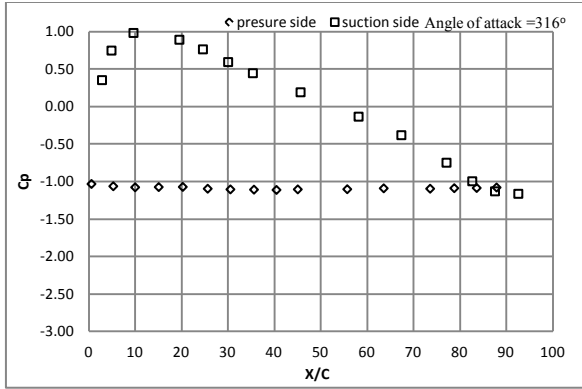


Figure 15(i): Pressure Distribution over the aerofoil for angles of attack from 316 to 336 degree

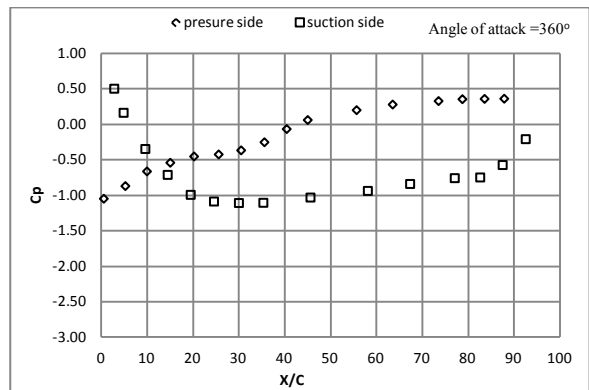
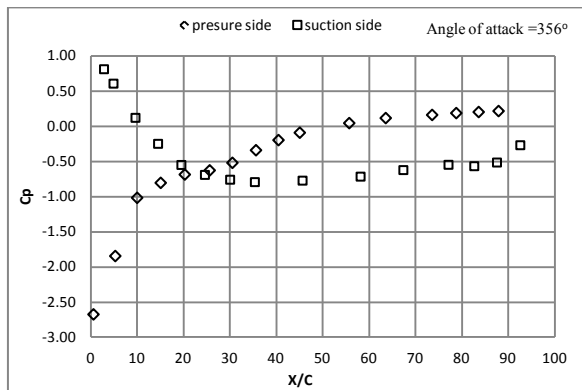
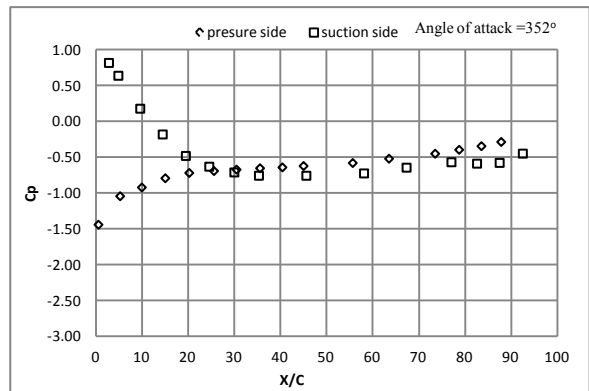
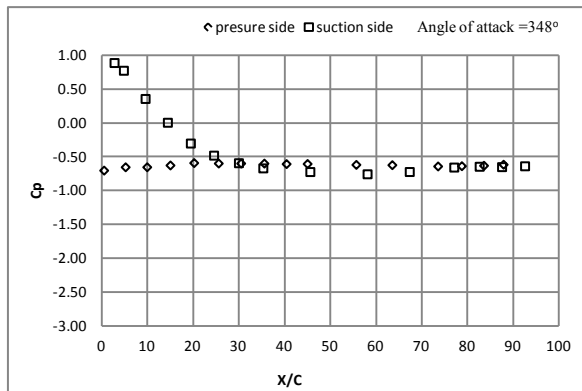
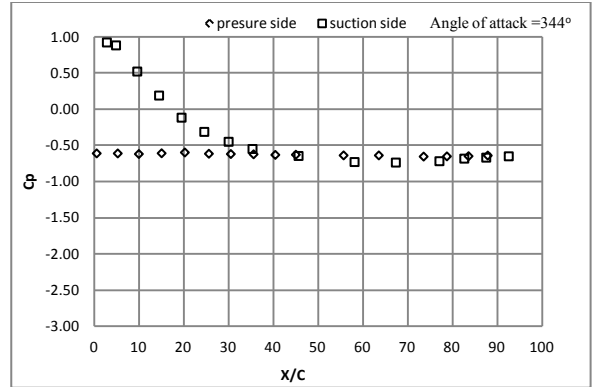
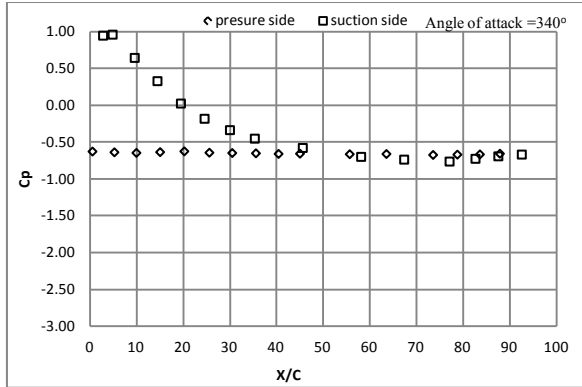


Figure 15(k): Pressure Distribution over the aerofoil for angles of attack from 340 to 360 degree

3. Cp plot for variable angles attack NWT 2005

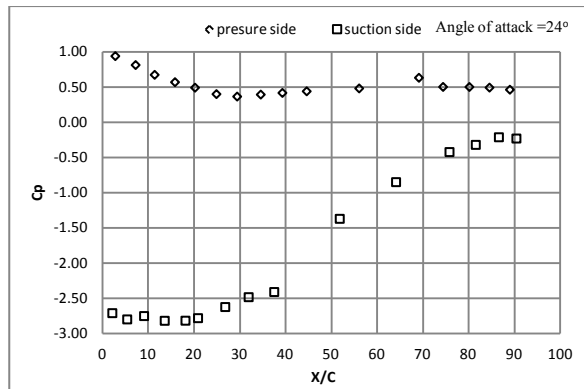
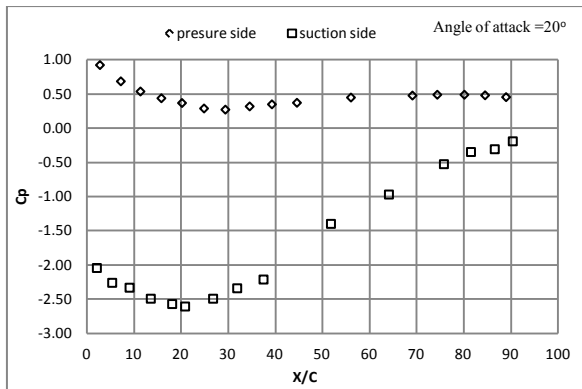
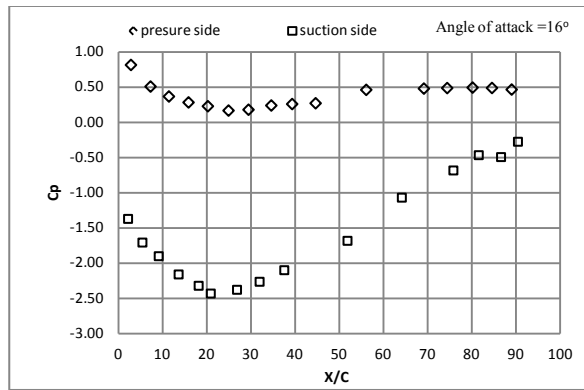
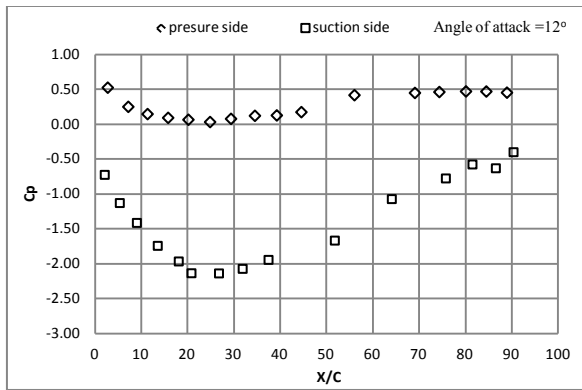
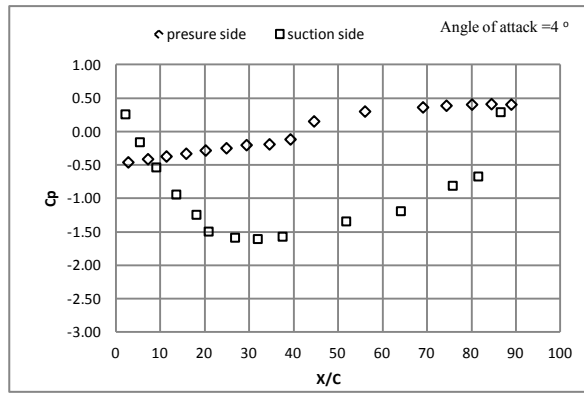
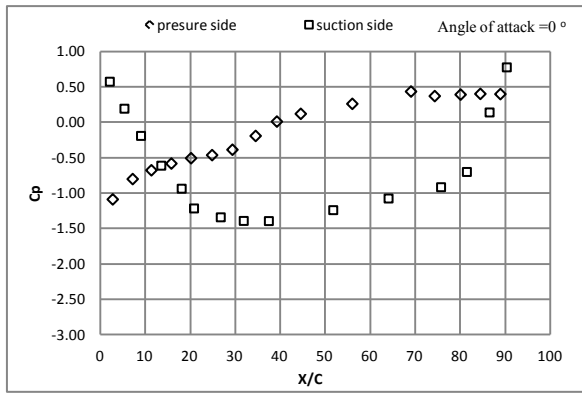


Figure 16(a): Pressure Distribution over the aerofoil for angles of attack from 0 to 24 degree

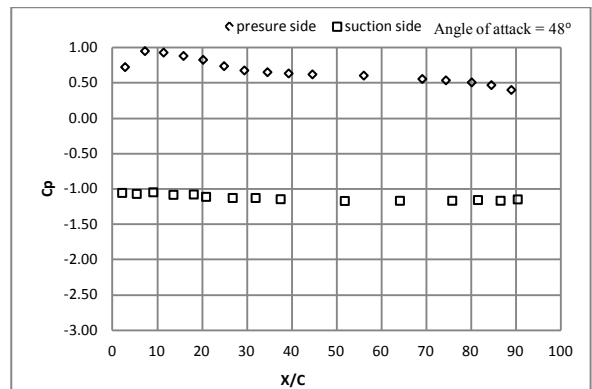
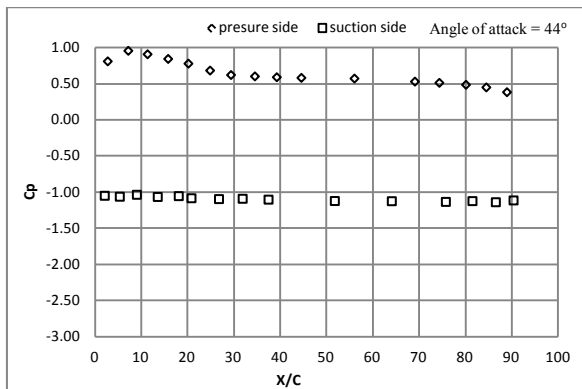
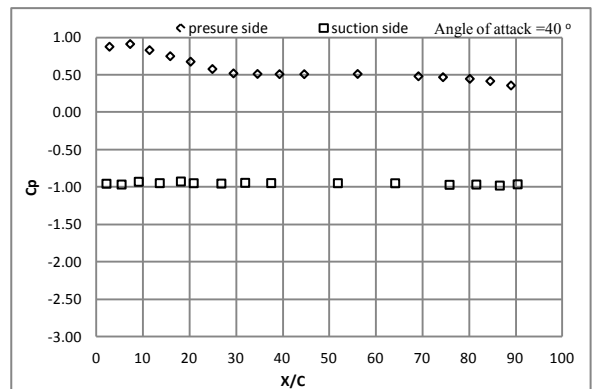
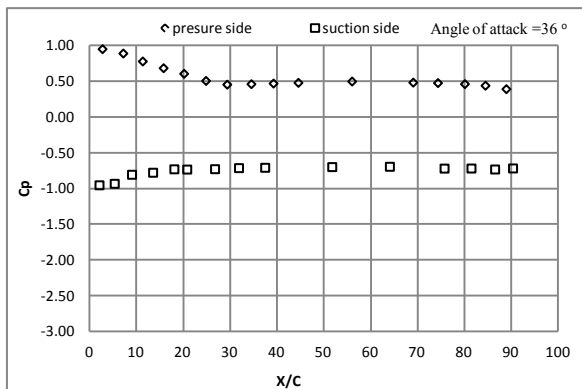
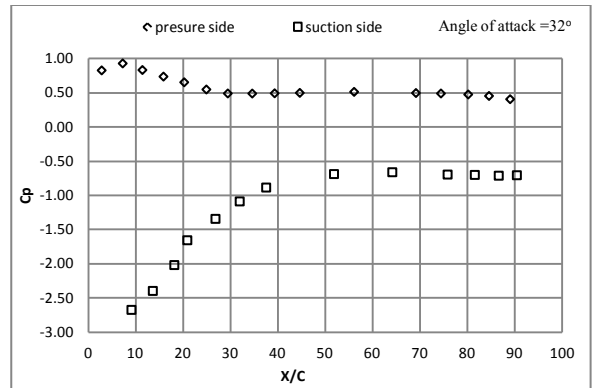
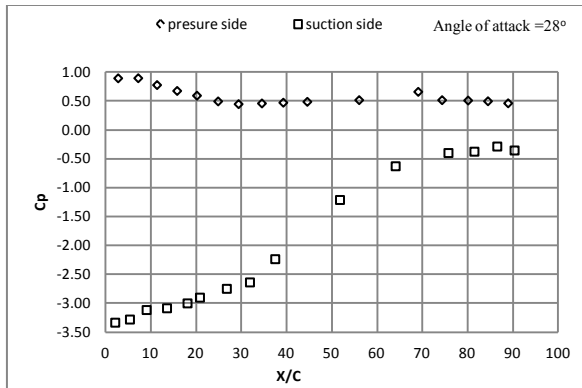


Figure 16(b): Pressure Distribution over the aerofoil for angles of attack from 28 to 48 degree

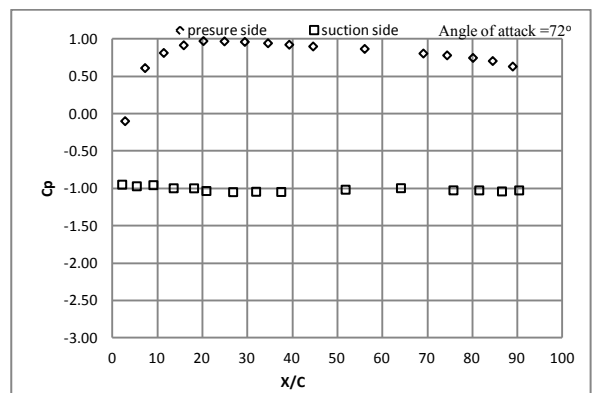
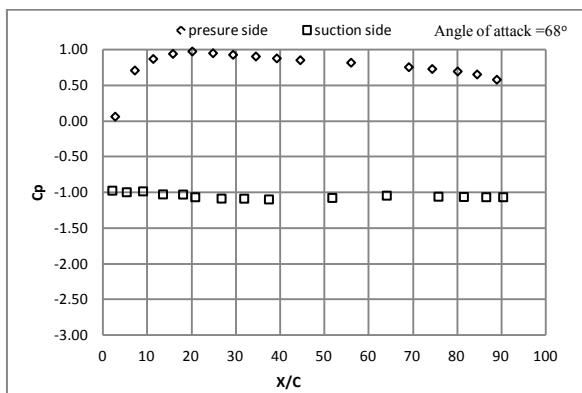
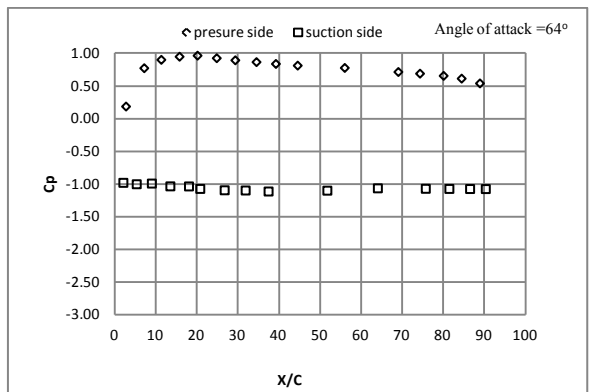
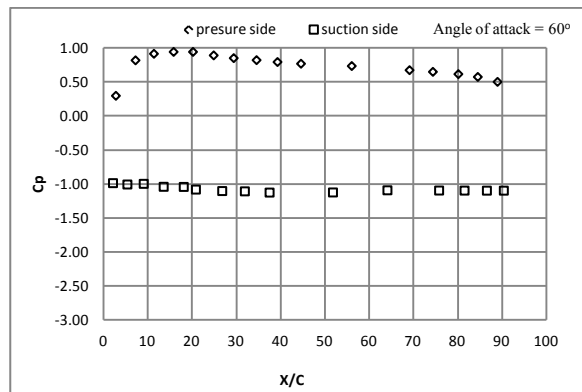
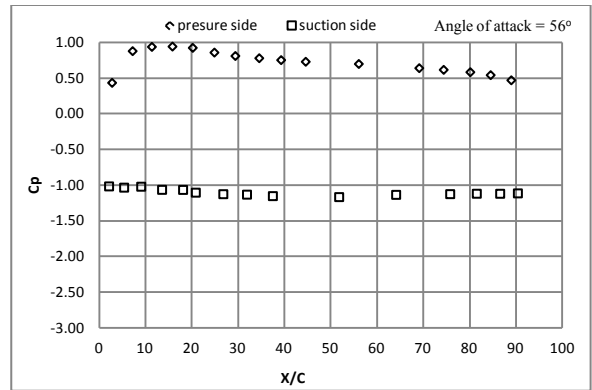
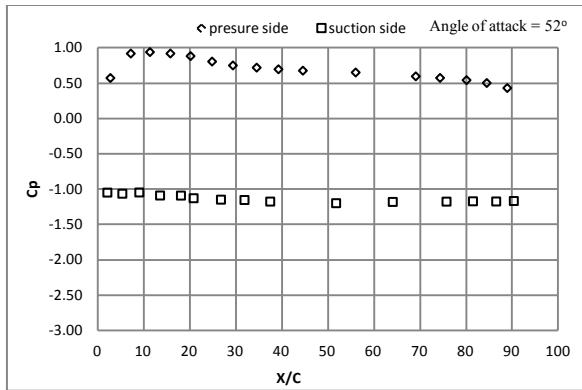


Figure 16(c): Pressure Distribution over the aerofoil for angles of attack from 52 to 72 degree

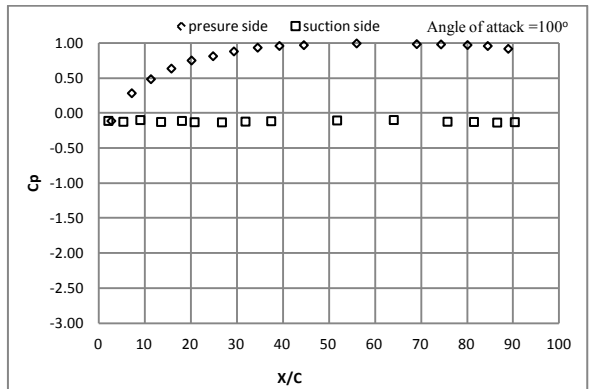
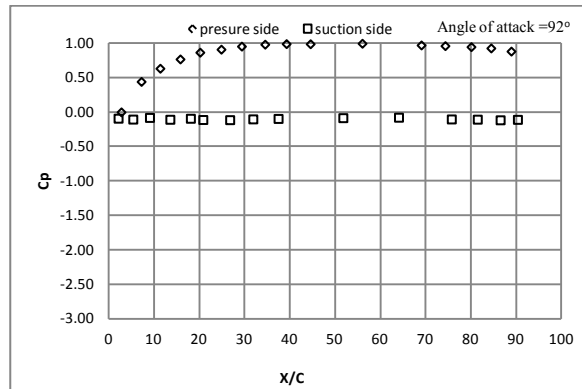
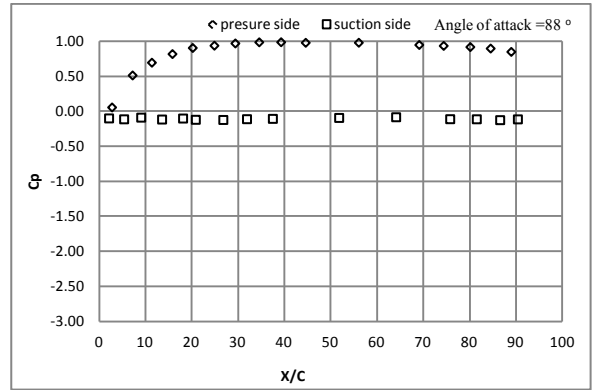
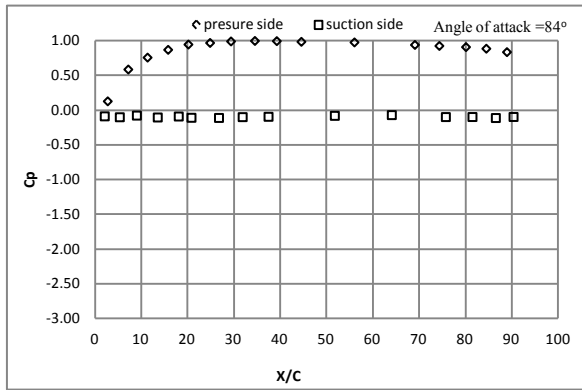
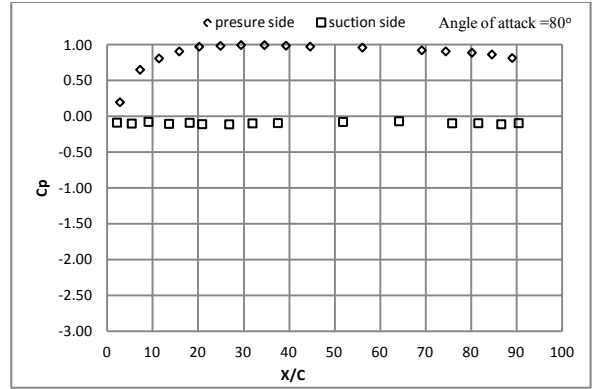
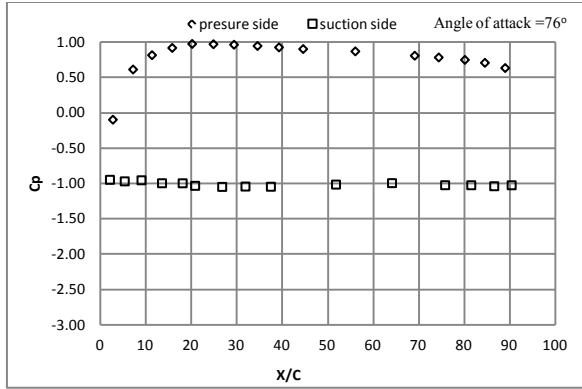


Figure 16(d): Pressure Distribution over the aerofoil for angles of attack from 76 to 100 degree

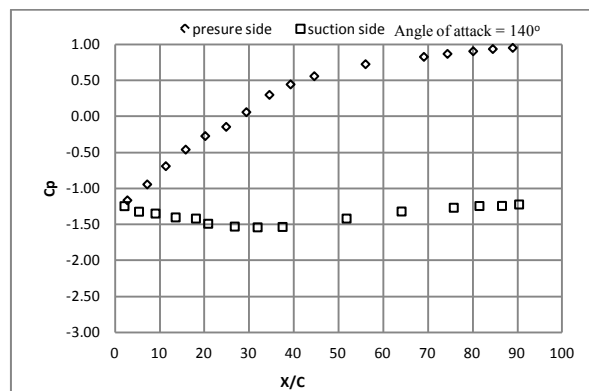
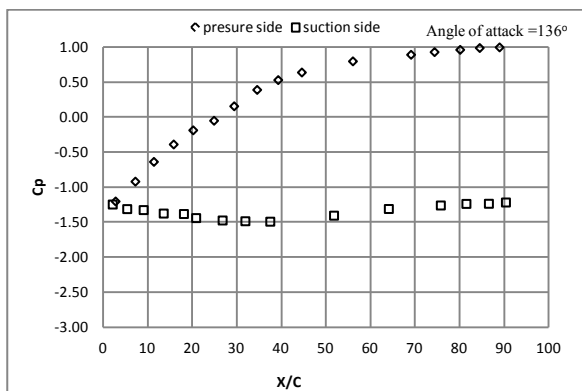
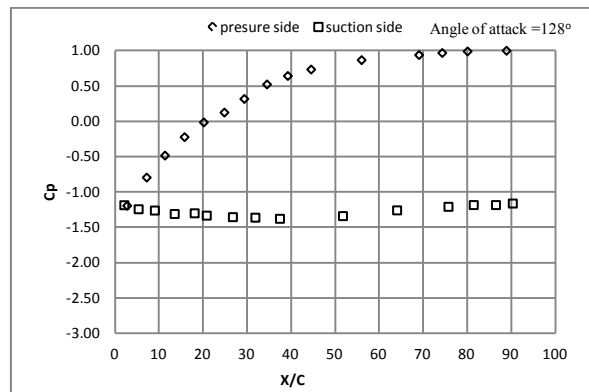
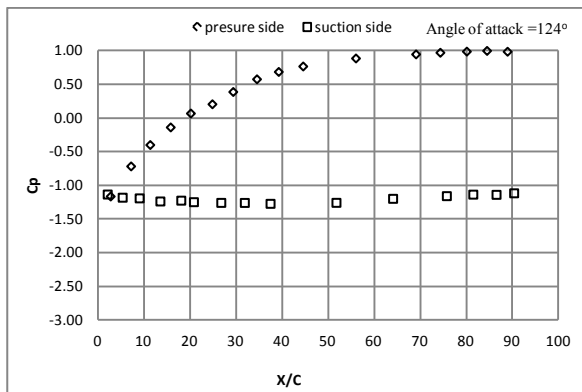
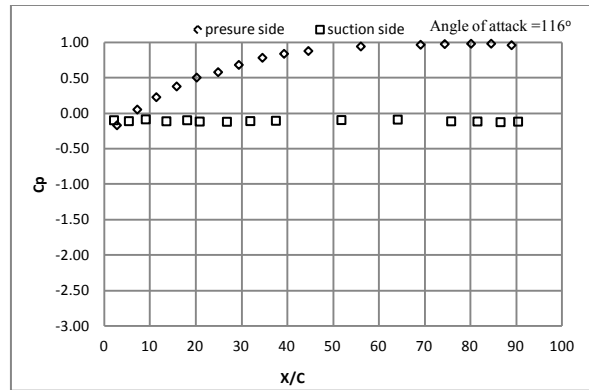
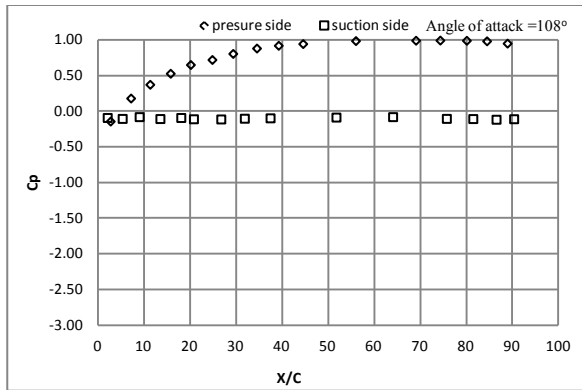


Figure 16(f): Pressure Distribution over the aerofoil for angles of attack from 108 to 140 degree

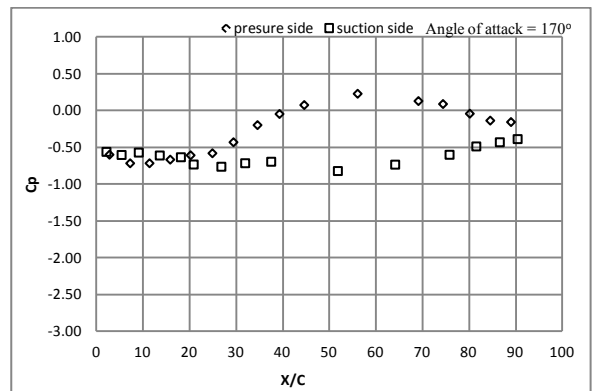
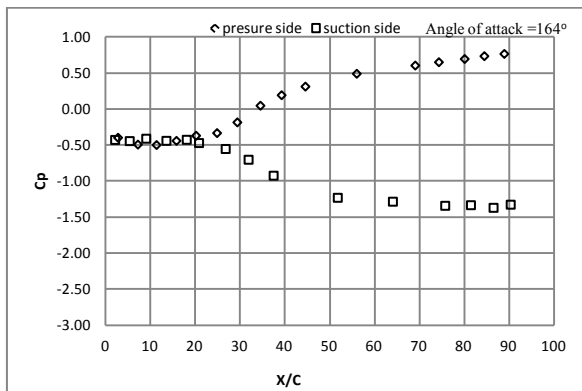
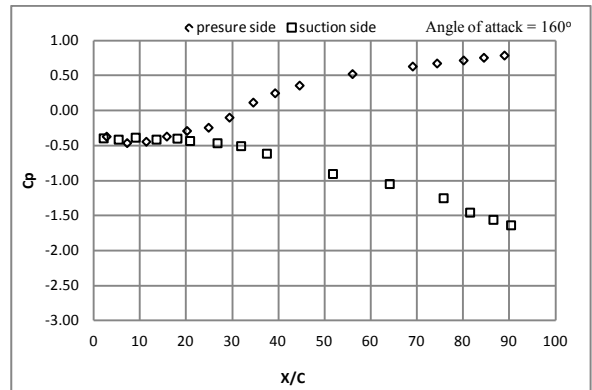
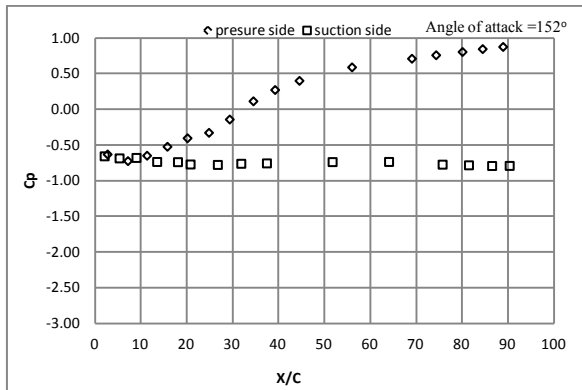
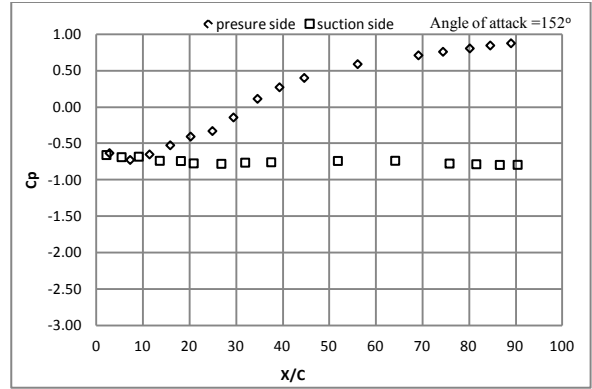
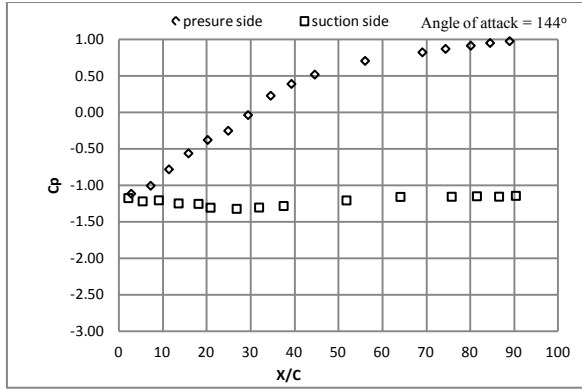


Figure 16(g): Pressure Distribution over the aerofoil for angles of attack from 144 to 170 degree

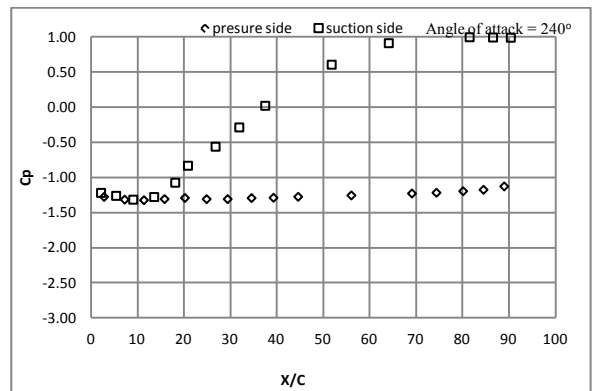
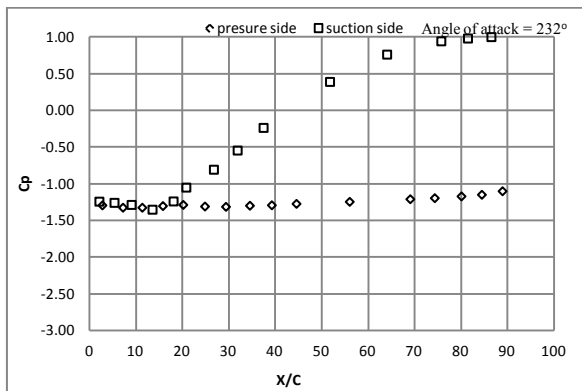
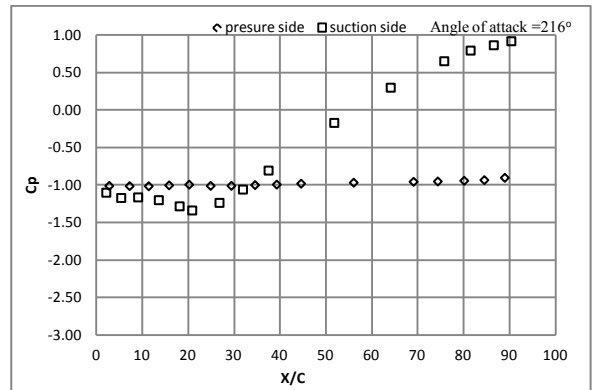
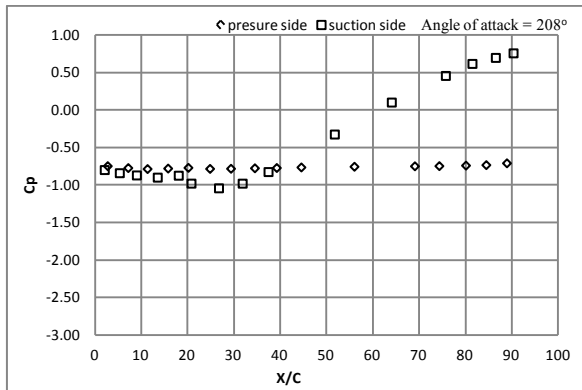
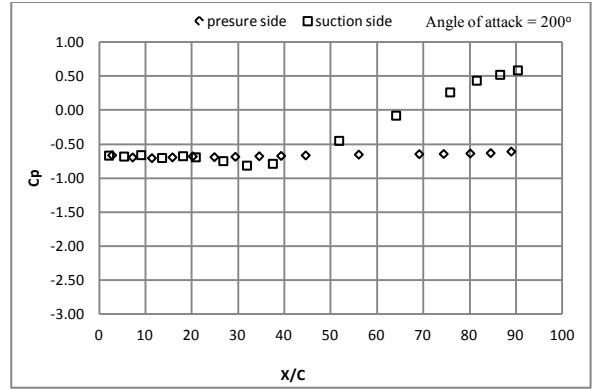
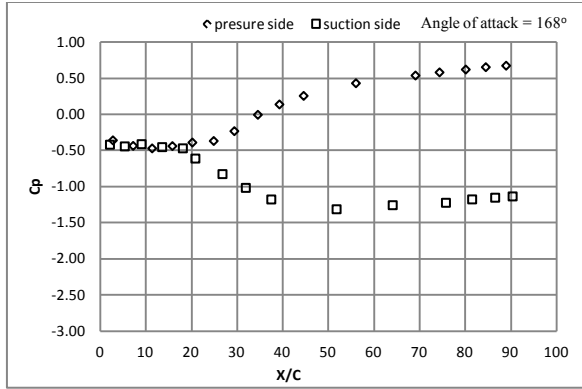


Figure 16(h): Pressure Distribution over the aerofoil for angles of attack from 168 to 240 degree

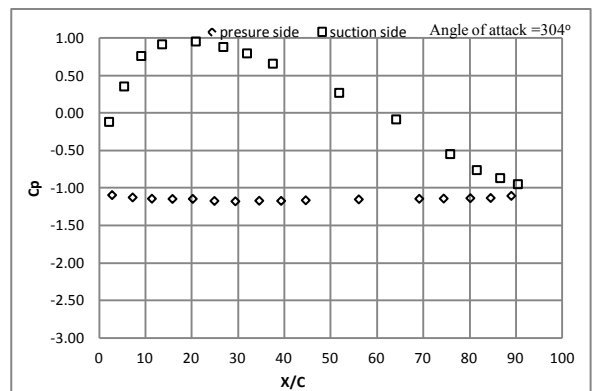
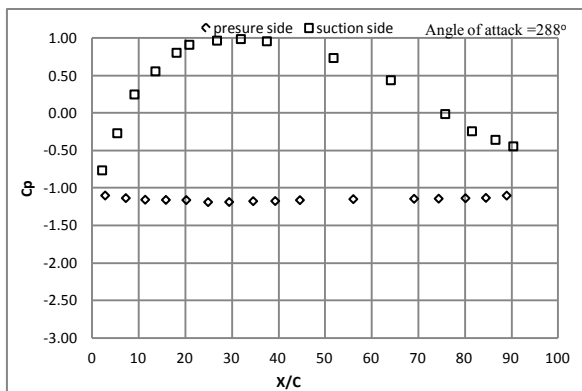
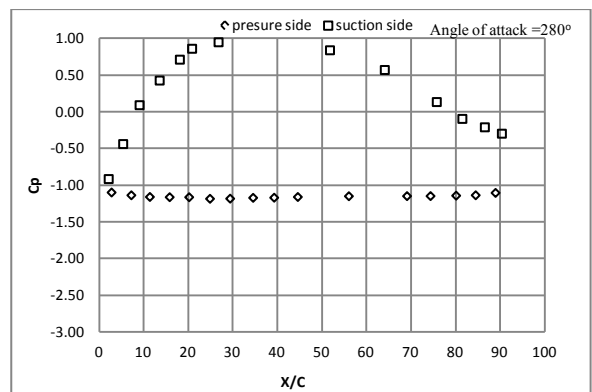
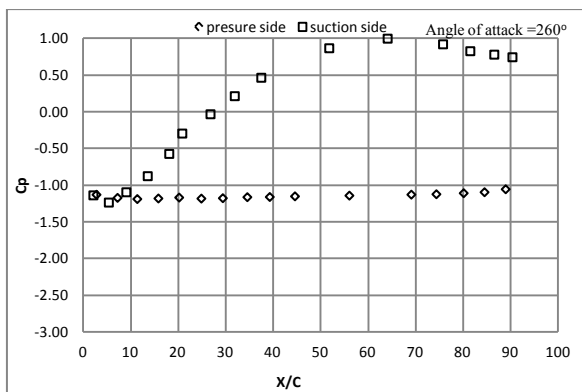
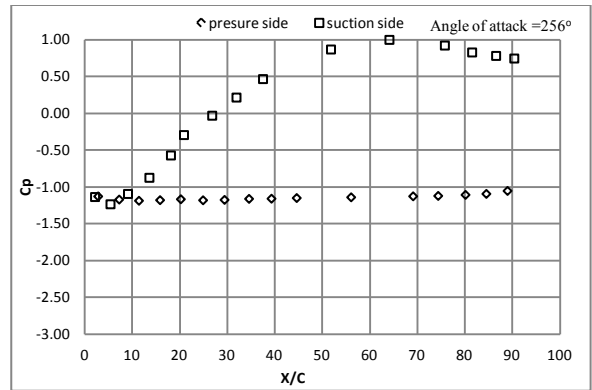
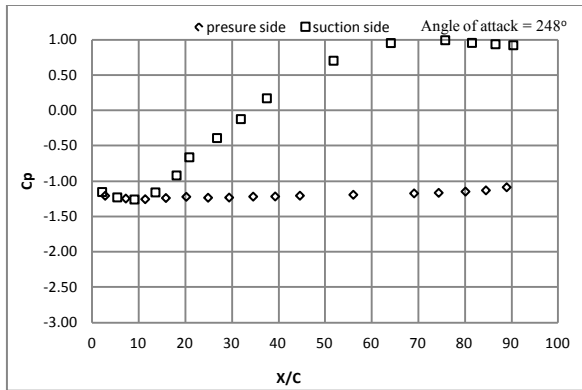


Figure 16(i): Pressure Distribution over the aerofoil for angles of attack from 248 to 304 degree

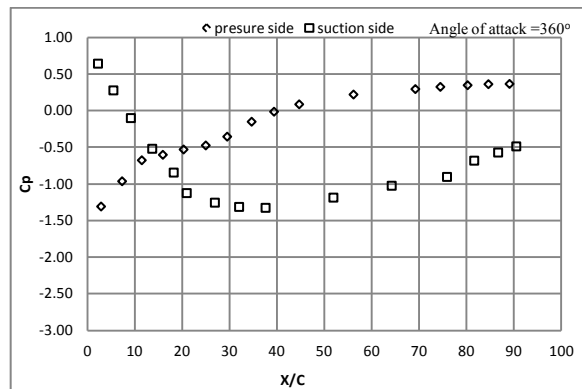
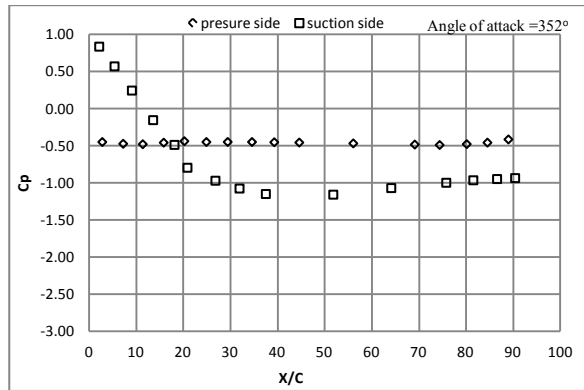
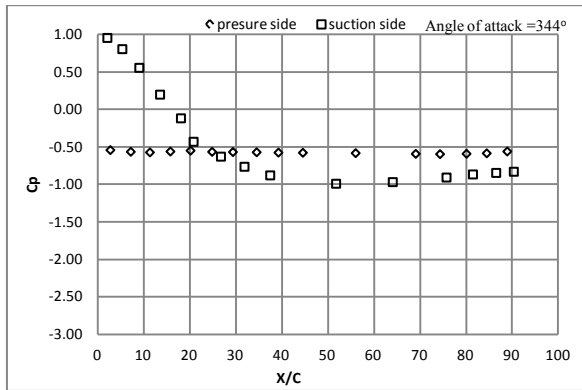
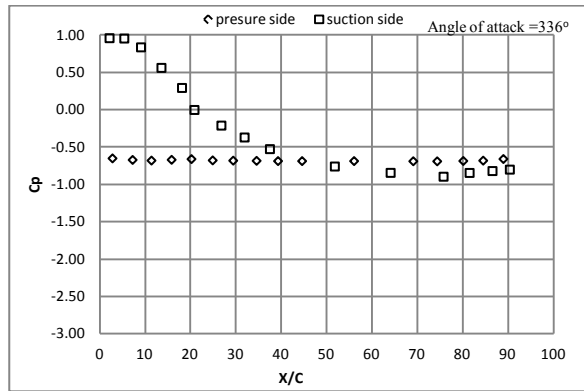
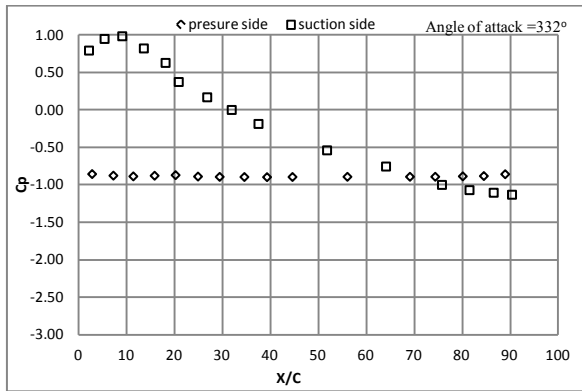
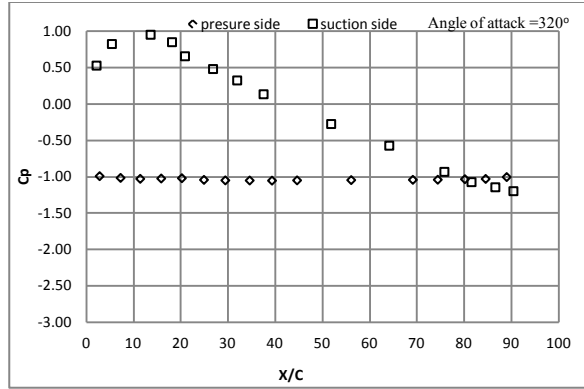
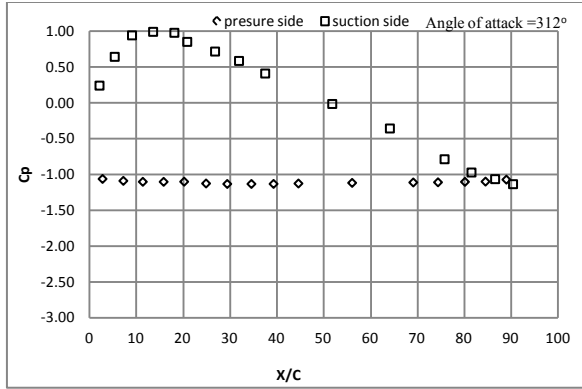


Figure 16(j): Pressure Distribution over the aerofoil for angles of attack from 312 to 360 degree

REPORT DOCUMENTATION PAGE

<p>TITLE</p> <p align="center">Experimental characteristics of wind turbine blading over full 0 to 360 degree angle of attack</p>	<p>RTQIGEV NUMBER/DATE TF/TF/622/33,'Cpir1 2014</p>
<p>AUTHOR(S)</p> <p align="center">A.P.Haran and S.Soundranayagam</p>	
<p>PERFORMING ORGANIZATION/DEPARTMENTS</p> <p align="center">Department of Aeronautical engineering PARK college of engineering and Technology Anna university, Coimbatore</p>	<p>No. of copies</p>
<p>OTHER PARTICIPATING ORGANIZATION/DEPARTMENTS</p>	
<p>SPONSORING AGENCY AND ADDRESS</p> <p align="center">Centre for Wind Energy Technology- Chennai (C-WET)</p>	<p>SPONSORING AGENCY</p>
<p>SUPPLEMENTARY NOTES</p> <p align="center">Centre for Wind Energy Technology</p>	<p>DISTRIBUTION/AVAILABILITY STATEMENT</p> <p>Unrestricted</p>
<p>ABSTRACT</p> <p>A well designed wind turbine should have a good low speed starting characteristics and an optimum performance at rated wind speed. This depends on the knowledge of the aerofoil characteristics over 360 degree angle of attack and a detailed aerodynamic behavior of flow around wind turbine aerofoils in the regions immediately before and after stall. It is also necessary to detect the stall hysteresis, if any, in the chosen profiles. This report summarizes the experimental work done on three wind turbine blade profiles designed by National Aerospace Laboratories Bangalore for a given wind turbine power generation system. The 2D blades have been manufactured with pressure tapings and tested at angles of attack varying from 0° to 360° to generate pressure distribution in PARK airflow laboratory. Based on the pressure distribution, aerodynamic characteristic viz. Cl and Cd have been estimated at a Reynolds number of 200 000 for all angles of attack ranging from 0° to 360° for the three profiles. Deep stall hysteresis has been captured in all three cases. The results indicate that the wind turbine profiles have been chosen to have a good starting characteristics and good performance at rated wind speed. The operation of the turbine is such that it avoids regions having hysteresis.</p>	
<p>SUBJECT TERMS</p>	